POSTSEISMIC DEFORMATION FOLLOWING THE 1991 RACHA, GEORGIA EARTHQUAKE

by

Joel Edwin Podgorski

B.S., University of California at Santa Cruz, 1997

A THESIS SUBMITTED IN PARITAL FULFILLMENT OF
THE REQUIREMENTS FOR THE DEGREE OF

MASTER OF SCIENCE

in

THE FACULTY OF GRADUATE STUDIES

(Geophysics)

THE UNIVERSITY OF BRITISH COLUMBIA

July 2006

©Joel Podgorski, 2006

Abstract

The April 29, 1991 Racha, Georgia M_w=6.9 earthquake was the largest earthquake recorded in the western section of the Greater Caucasus Mountains. Lithospheric deformation following this earthquake was recorded by a network of eight GPS stations. These data were modeled for postseismic deformation with the mechanisms of afterslip and viscoelastic relaxation. Prior to modeling, the GPS data were corrected for secular tectonic motions by two separate methods. The first was to use the 1996-2000 portion of the GPS time-series as an estimate of preseismic deformation rates. The second method involved using a regional tectonic block model to produce velocity estimates for the GPS stations. Shallow afterslip was found to best explain the data for the 1991-1994 time period with a moment of 7×10^{18} N m. This is equivalent to about 20% of the coseismic moment and represents 300 times the total moment released from aftershocks during the same time period. Most of the postseismic deformation was completed by 1994. While viscoelastic relaxation was not found to be responsible for postseismic deformation, it was determined that viscosities less than 10^{18} Pa sec can be ruled out for possible a possible viscoelastic layer in the lower crust.

Contents

Abstract ii

Contents iii

List of Tables vi

List of Figures viii

1 Introduction 1

2 Background 3

2.1 Tectonic Setting 3

2.2 Geology 6

2.3 Lithospheric Structure 7

2.4 Seismicity 9

3 Racha Event 11

4 Postseismic Deformation Processes 14

4.1 Fault Afterslip 15
4.2 Viscoelastic Relaxation 19
4.3 Other Postseismic Processes 21

5 Other Postseismic Deformation Studies **24**

6 GPS Data **28**
6.1 Stations and Time Points 29
6.2 Acquisition 30
6.3 Analysis 31
6.4 Position Measurements 31
6.5 Velocity Decay in GPS Time-Series 33
6.6 Secular Correction 37
6.7 Error Combination 42
6.8 Data Used in Modeling 42

7 Methods **44**
7.1 Afterslip Inversion Modeling 44
7.2 Viscoelastic Forward Modeling 48

8 Results **53**
8.1 Afterslip 53
8.2 Viscoelastic Relaxation Modeling 70

9 Discussion **75**

9.1 Secular Correction of GPS Data 75
9.2 Afterslip and Viscoelastic Relaxation Models 77

10 Conclusions **83**

Bibliography **85**

Appendix A GPS Position Measurements **95**

Appendix B Conversion Velocities for ITRF2000 to Eurasian Reference Frame **98**

Appendix C GPS Displacements **99**

Appendix D Earth Model for Viscoelastic Modeling **102**

List of Tables

2.1 Crustal P and S wave velocities from Triep et al (1995) compared with typical P and S velocities from the PREM (*Dziewonski and Anderson*, 1981). 8

3.1 Racha source parameters according to different sources. Moment is listed with total coseismic moment above and mainshock-only moment below in parentheses. 12

6.1 Study duration, number of GPS stations, and average number of observations of other postseismic deformation studies. 29

6.2 Residuals (WSTD) and linear rates from linear and logarithmic functions fit to data. Amplitude of logarithmic function is also included. All values are in mm or mm/yr. 36

6.3 Block model velocities (mm/yr) used in correcting GPS time-series for secular tectonic displacements. 42

7.1 Coseismic slip on 4 km × 4 km fault patches from model of Tan (2005). 52

8.1 Sensitivity of afterslip results to choice of fault plane as measured by changes in WRSS reduction explained by inversion models. Inversions are based on TSC data and a β (smoothing) of 10 km^2/m. Fault geometries begin with the parameters of Tan (2005) and are adapted incrementally to the models of (a) Fuenzalida et al (1997), (b) Triep et al (1995), and (c) Harvard CMT. 60

8.2 Comparison of WRSS reduction and moment resulting from models with different β values. The first two β values for each data set are those determined by the methods of analyzing the trade-off between misfit and roughness and of cross validation sum of squares (CVSS). The third β value, a more conservative 10 km^2/m, is that which was used in many of the tests presented in the results. This value had been chosen due to it allowing for a more reasonable-appearing slip distribution. 65

8.3 Test for the sensitivity to Poisson's ratio, ν, by increasing and decreasing ν from the value of 0.25 otherwise used. Differences in WRSS reduction and moment are indicated. 68

List of Figures

1.1 Generalized tectonic setting of the Caucasus Mountain region. The Anatolia and Azerbaijan blocks displace to the west and east respectively while the Arabian plate proceeds northward into Eurasia (Lesser and Greater Caucasus). 2

2.1 Selected large-scale tectonic and geologic features of the Caucasus Mountains. MCT is the Main Caucasus Thrust. GDZ is the Gagra-Dzhava Zone of Jurassic sedimentary rocks just north of the Racha epicenter which is indicated by a star. DM is the crystalline Dzirula Massif on the south side of the Racha epicenter. BKSZ is the Borzhomi-Kazbeg Shear Zone. 5

4.1 Rate and state friction. Friction, μ, is represented in the vertical direction and displacement in the horizontal direction. a is the increase in friction due to a sudden acceleration, and b is the decrease from this peak by the end of the period of greater speed. $a - b$ determines if a medium experiences (a) velocity weakening (negative) or (b) velocity strengthening (positive). 17

6.1 Location of GPS sites (triangles). Solid rectangle indicates the modeled coseismic slip plane and star the epicenter of Tan (2005), and dashed plane indicates rectangle of afterslip plane. 30

6.2 Map of part of the tectonic block model used in producing secular velocity estimates (*Reilinger et al*, 2006). The area of this study as well as the straight line estimate of the Main Caucasus Thrust plate boundary are indicated. 40

7.1 Profile perpendicular to strike of afterslip fault plane with geometry of Tan (2005) and two months of aftershocks. 47

7.2 Coseismic fault model, from Tan (2005). Displacement is in meters. Each tile is 4 km square. 47

7.3 Fault plane resolution tests using alternating 1 and 0 meter slip patches on a 120 km × 40 km plane. (a) 60 km × 20 km and (b) 20 km × 20 km sized slip patches were forward modeled (top) and the resulting surface displacement vectors were inverted for slip (bottom) to determine which areas of the modeled fault plane the GPS network can resolve slip on. Inversions were performed using a smoothing, β, of 10 km^2/m except where indicated. 49

8.1 1991-1994 afterslip inversion results using (a) TSC data and (b) BMC data. (c) Coseismic slip model of Tan (2005). Star on each slip plane represents the Racha hypocenter, and each tile is 4 km square. Comparing either afterslip model (a) or (b) with the coseismic slip model (c) shows that the bulk of modeled afterslip occurs away and up-dip from the area of maximum coseismic slip. 54

8.2 Comparison of 1991-1994 data vectors with 1-σ error ellipses (red) with model vectors (blue). Model vectors are produced by forward modeling the afterslip results. (a) is from using TSC data and (b) is from using BMC data. The star represents the Racha epicenter. . . . 55

8.3 1991-1994 slip inversion using data with no secular correction. WRSS reduction is 51.7435% and the moment is 8.987 ×10^{18} N m. 56

8.4 1991-1994 afterslip model and data vectors for all available sites for (a) TSC data (b) BMC data and (c) non-corrected (NC) data. 57

8.5 1991-1994 slip inversions using the same GPS sites for all data sets (without site NICH). (a) TSC model (b) BMC model (c) NC model. 58

8.6 Surface outline of the fault plane using the fault geometries of Tan, Fuenzalida, Triep, and Harvard CMT. Stars are the Racha epicenter according to the different groups. 61

8.7 Patterns of modeled afterslip using different published fault geometries. Star indicates the Racha hypocenter. (a) Tan (2005), (b) Fuenzalida et al (1997), (c) Triep et al (1995), (d) Harvard CMT. 62

8.8 Determination of smoothing parameter, β, for TSC data (a,b) and BMC data (c,d). The first method used, a "Tikhonov plot", determines where the change between the weighted residual sum of squares (WRSS) and roughness is greatest (a,c) and then use the associated β. The second method is cross validation sum of squares (CVSS) where β is chosen based on which value produces the smallest sum of residuals. Between the two methods, the optimal value of β ranges from 2 to 4 km^2/m for the TSC data and 3 to 7.5 km^2/m for the BMC data. 66

8.9 Afterslip inversions resulting from use of different smoothing values, β, for TSC and BMC data. The first two smoothing values displayed for each data type are those corresponding to the methods of WRSS versus roughness and of CVSS (see Figure 8.8). 67

8.10 1991-1994 afterslip inversions with dip-slip and strike-slip components using (a) TSC data and (b) BMC data. 69

8.11 1994-1996 afterslip inversion results (a) using data TSC data and (b) using BMC data. Star on each slip plane represents the Racha hypocenter, and each tile is 4 km square. 70

8.12 Sensitivity of WRSS to lower-crust viscoelastic layer thickness and viscosity. The best model with the TSC data (a) has a viscoelastic lower crust of 10 km thickness and a viscosity of about 1.0×10^{17} Pa sec. The best model (star) with BMC data (b) has a viscoelastic lower-crustal thickness of 10-18 km and a viscosity of about $2.5 - 6 \times 10^{17}$ Pa sec. 71

8.13 Displacement vectors from best fitting Visco1D models and 1991-1994 GPS site displacements. (a) TSC data with a viscoelastic lower crust at 35-45 km with a viscosity of 1×10^{17} Pa sec. (b) BMC data with a viscoelastic lower crust at 25-45 km with a viscosity of 9×10^{17} Pa sec. Star is the Racha epicenter. 72

8.14 WRSS versus logarithm of viscosity for forward-modeled viscoelastic mantle half-space models compared with (a) TSC data and (b) BMC data. 73

8.15 Comparison between BMC data and models of a 20 km thick viscoelastic lower crust (25-45 km depth). (a) WRSS versus logarithm of viscosity. (b) Corresponding WRSS reduction versus logarithm of viscosity. 74

9.1 (a) Aftershocks over the two months following the Racha event (May 10, 1991 to July 9, 1991) (*Fuenzalida et al*, 1997). Afterslip fault plane is outlined. Star represents Racha hypocenter and can be used with fault plane outline to compare aftershocks with 1991-1994 (b) TSC afterslip and (c) BMC afterslip. The afterslip models are from data covering the period July 25, 1991 to October 10, 1994. 80

Chapter 1

Introduction

The April 29, 1991 Racha, Georgia M_w=6.9 earthquake was the largest recorded earthquake in this western section of the Greater Caucasus Mountains. This region comprises a section of the complex Arabian-African-Eurasian plate collision zone. Soon after the earthquake eight Global Positioning System (GPS) stations were deployed in and around the earthquake rupture area. The focus of this study is the use of measurements from these GPS stations to constrain models that describe accelerated crustal deformation resulting from this earthquake. A reason for doing this is to place constraints on what deformation mechanisms and rheologies may exist in this part of the continental collision zone. This knowledge will help create a clearer picture of the mechanisms at work in this plate boundary zone in particular and in continental collision zones in general.

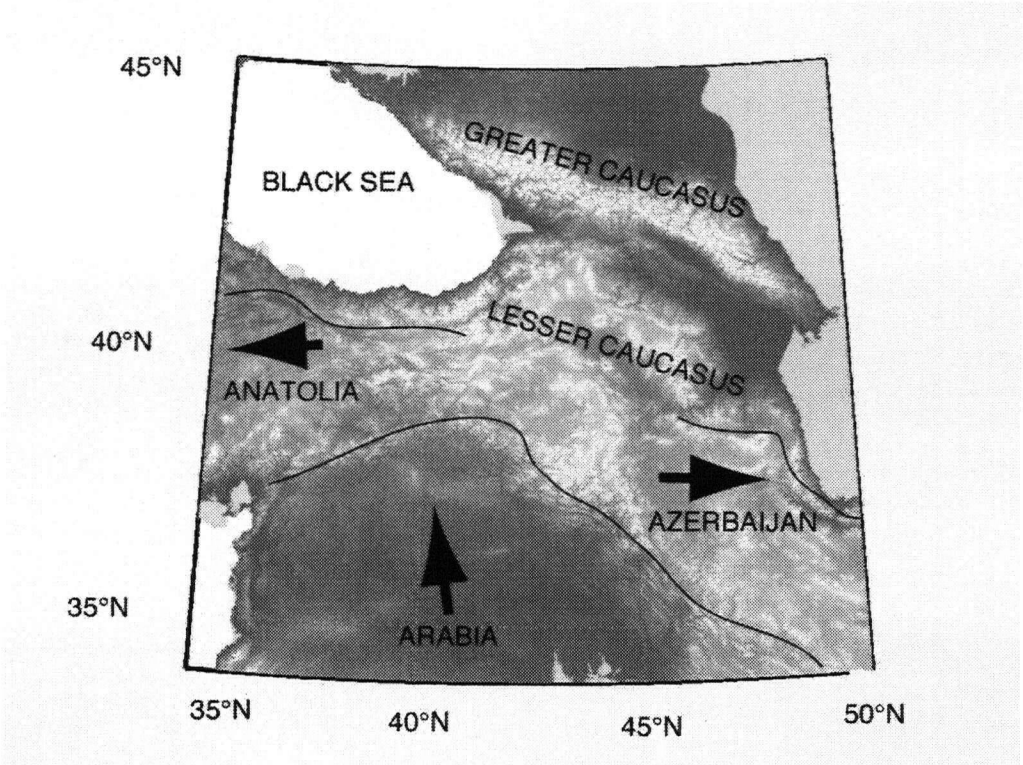

Figure 1.1: Generalized tectonic setting of the Caucasus Mountain region. The Anatolia and Azerbaijan blocks displace to the west and east respectively while the Arabian plate proceeds northward into Eurasia (Lesser and Greater Caucasus).

Chapter 2

Background

2.1 Tectonic Setting

The Caucasus Mountains are contained within the northern part of the middle segment of the Alpine-Himalayan fold belt and are created by the collision of Arabia into Eurasia (e.g., *McKenzie*, 1970) (Figure 1.1). This results in both the Greater and Lesser Caucasus being under a compressional stress regime (*Philip et al*, 1989). The Caucasus Mountains are bounded on the west and east by oceanic crust of the Black Sea and South Caspian basins respectively and are formed by many nappes thrust generally from north to south. Exceptions to this include northward (in addition to southward) thrusting in the eastern Greater Caucasus and in the far western portion of the western Greater Caucasus. The region contains a string of recent volcanic features that are aligned roughly N-S from the Arabian plate to the Greater Caucasus, suggesting E-W extension

(*Fuenzalida et al*, 1997). In particular there is a cluster of weak seismicity at 41.5°N, 44°E in the Lesser Caucasus that corresponds to N-S trending tensile volcanic fractures (*Philip et al*, 1989).

The Eurasian and Arabian plates converge at a rate of 25 ± 3 mm/yr along N20°W near the Caucasus (at 38°N, 40°E) (*DeMets et al*, 1990; *DeMets*, 1994; *Smith et al*, 1994; *Reilinger et al*, 1997; *Reilinger et al*, 2006). Subduction of continental crust is believed to be avoided by lateral extrusion of the Anatolian block, Azerbaijan block, and northwest Iranian block (*McKenzie*, 1972; *Jackson*, 1992) and by underthrusting of accreted terrains (*Triep et al*, 1995).

The oblique convergence relative to the Caucasus can be explained by two models: 1- indenter tectonics requiring a left-lateral strike-slip zone along the western boundary of the collisional region at the Borzhomi-Kazbeg shear zone (BKSZ) (*Philip et al*, 1989). (See Figure 2.1) 2- oblique convergence partitioned between Caucasus-perpendicular collision along this range and right-lateral motion along ESE-WNW faults further south (*Jackson*, 1992).

The BKSZ may be followed southwest into the Northeast Anatolian Fault. In the Greater Caucasus the shear zone splits into several segments, most notably along the Kazbeg volcano and also along the western end of the Alazani Basin (*Fuenzalida et al*, 1997).

There are many differences between the western and eastern Greater Caucasus, divided by the BKSZ at around 44°E. Philip et al (1989) point out the following. The western Greater Caucasus has concentrated deformation along its southern slope but simply a smooth monocline on its northern slope while

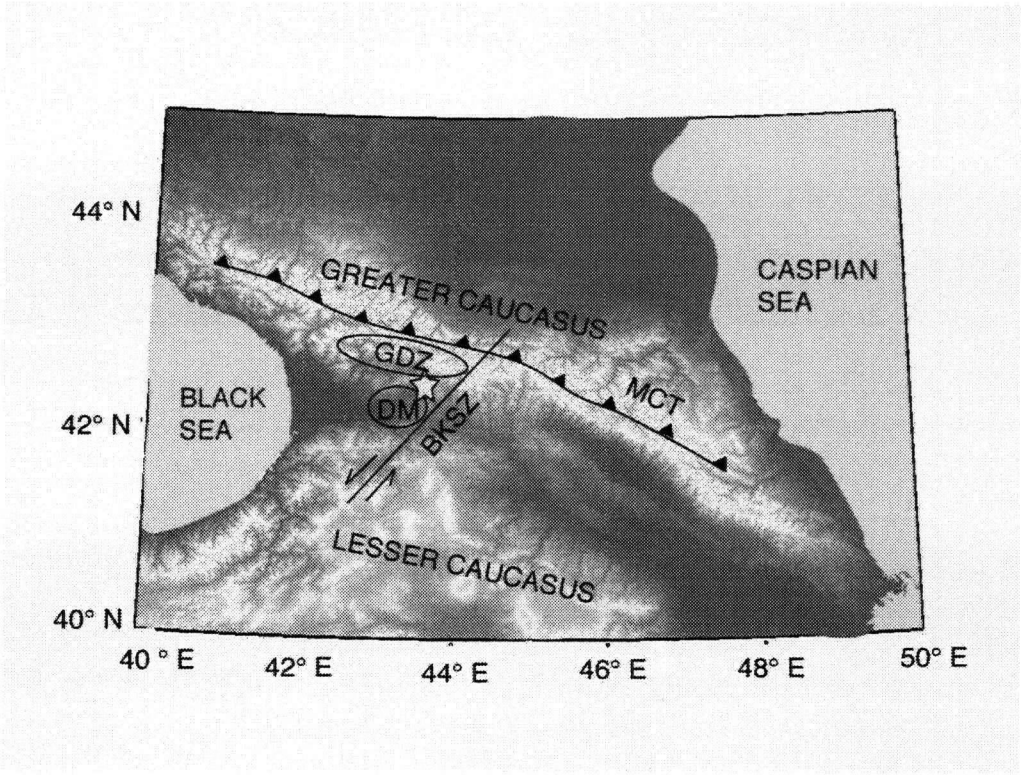

Figure 2.1: Selected large-scale tectonic and geologic features of the Caucasus Mountains. MCT is the Main Caucasus Thrust. GDZ is the Gagra-Dzhava Zone of Jurassic sedimentary rocks just north of the Racha epicenter which is indicated by a star. DM is the crystalline Dzirula Massif on the south side of the Racha epicenter. BKSZ is the Borzhomi-Kazbeg Shear Zone.

the eastern Greater Caucasus has concentrated deformation on both sides. Plio-Quaternary volcanism occurs only in the western Greater Caucasus (from Elbrus to Kazbek). Thrust faults on the northern boundary of the western Greater Caucasus dip to the south while those on the northern boundary of the eastern Greater Caucasus dip to the north. There is much more seismicity in the eastern Greater Caucasus, and the Racha event represents the largest known event

in the west. Intermediate depth earthquakes are found in the eastern Caucasus (possibly related to the remnant of a subducted slab (*Triep et al*, 1995)) but not in the western Caucasus (where there is Quaternary volcanism that could also indicate recent subduction). Bouguer gravity anomalies and topography suggest a northward displacement of the eastern Greater Caucasus relative to the western part (*Ruppel and McNutt*, 1990). Finally, unroofed basement is exposed in the west but not in the east (*Triep et al*, 1995).

2.2 Geology

The highest peaks in the Greater Caucasus, Elbrus and Kazbek, are located in the western part of the range and are Pliocene-Pleistocene volcanoes of calc-alkaline composition that have been active from late Miocene until historical times (*McKenzie*, 1972). The core of the Greater Caucasus's Main Range consists of highly metamorphosed Precambrian rocks (790 Ma) that are considered the remnants of a microcontinent. The northern Peredovoy Range contains Paleozoic ophiolites and island-arc complexes that represent a suture zone (*Zonenshain et al*, 1990).

The majority of the Greater Caucasus is underlain by Jurassic and Cretaceous rocks. The lower and middle Jurassic sequences are mostly shales and slates with the shale sequences containing lava layers up to 3 km thick. The oldest of these lavas is of calc-alkaline composition and is a remnant of a Great Caucasian island arc. Abundant basalts from the early and middle Jurassic occur in the

middle Greater Caucasus and are associated with rhyolite. This basalt-rhyolite series is interpreted to show the formation of the Great Caucasian sedimentary basin by extension (*Zonenshain et al*, 1990).

On the southern side of the Greater Caucasus, continuous sedimentation is found from the middle Jurassic through the Cretaceous and Paleogene with no uplift and occurred in a marginal sea north of the Lesser Caucasus (*Kopp and Shcherba*, 1985). This shows that uplift of the Greater Caucasus began in the middle to late Miocene, and it has continued until the present. The rocks on the north side of the Racha rupture area are the Jurassic Gagra-Dzhava thrust sheet (*Triep et al*, 1995) (See Figure 2.1).

To the south of the Jurassic through Paleogene sequences is the crystalline Dzirula Massif that shows similarities to the late Paleozoic Hercynian structures in Europe (*Kopp and Shcherba*, 1995; *Dotduyev*, 1986) and is different from the Gondwanan microcontinents to the south. It is overthrust on the south by the Lesser Caucasus (*Burtman*, 1989) and on the north by the Greater Caucasus. Paleomagnetic data show an intermediate position between Eurasia and Gondwana (*Asanidze et al*, 1980).

2.3 Lithospheric Structure

It is uncertain exactly what the depth of the Moho is beneath the Greater Caucasus. Bouguer gravity studies indicate a Moho depth of up to 60 km (*Ruppel and McNutt*, 1990) with a depth of about 45 km in the vicinity of the Racha rupture

area (*Balavadze et al*, 1979). That is, once the effects of elevation and the mass of the mountains were accounted for, anomalously low gravity measurements implied a thicker than normal crust. As well, in their Racha source study Triep et al (1995) used a model borrowed from the Georgian Academy of Sciences with a Moho depth of 45 km (which they adapted to a 44 km depth), though it is unclear on what basis this model was formed.

Triep et al (1995) calculated crustal P and S wave velocities by inversion of P and S arrival times from the Racha mainshock and aftershocks. These are shown in Table 2.1 and are compared with crustal values of the Preliminary Reference Earth Model (PREM) (*Dziewonski and Anderson*, 1981). Triep et al's velocities are generally less than those of the PREM, suggesting a lower crustal density due to either less dense material, higher temperatures, or both.

Crustal P and S Velocities

	Triep et al		**PREM**	
Depth (km)	**P Velocity (km/sec)**	**S Velocity (km/sec)**	**P Velocity (km/sec)**	**S Velocity (km/sec)**
0 - 3	4.83	2.61	5.80	3.20
3 - 7	5.44	3.19	5.80	3.20
7 - 19	5.98	3.51	6.13	3.43
19 - 45	6.33	3.65	6.80	3.90

Table 2.1: Crustal P and S wave velocities from Triep et al (1995) compared with typical P and S velocities from the PREM (*Dziewonski and Anderson*, 1981).

An abrupt boundary in seismic attenuation of P and S waves exists between the stable Russian platform to the north and the Greater Caucasus (*Sarker and*

Abers, 1998). According to laboratory experiments the detected amount of attenuation corresponds to a temperature increase along the base of the crust of 70-400°C relative to the platform (*Kampfmann and Berckhemer*, 1985; *J. Jackson et al*, 1992). Sarker and Abers (1998) point out that if the attenuation is due to increased temperatures that lower densities would exist (for a given chemical composition) thereby rendering Bouguer gravity estimates of Moho depth inconclusive.

There is also tomographic attenuation evidence from *Pn* waves of a partially eroded to completely absent lithospheric mantle beneath the western Greater Caucasus (*Al-Lazki et al*, 2003). This suggests a thin lithosphere with little or no mantle component underlain by an upper mantle asthenosphere.

2.4 Seismicity

There have been several large earthquakes in or near the Caucasus Mountains during the latter part of the 20th century. The 1970 Dagestan thrust event (M_s=6.5) took place on the northern slope of the eastern Greater Caucasus. In 1988 the Spitak earthquake (M_s=6.9) occurred along the southern thrust of the Lesser Caucasus. The 1990 Manjil (Iran) earthquake (M_s=7.3) took place by the southwestern coast of the Caspian Sea and showed a left-lateral mechanism consistent with the expulsion of the northwest Iranian block. Another strike slip event (M_s=6.8) occurred in 1992 in Erzincan (Turkey) along the North Anatolian Fault. In general, in the Greater Caucasus seismicity is concentrated along

its southern boundary where surface elevations are less and deformation is able to more easily occur (*Allen et al*, 2004).

Chapter 3

Racha Event

The M_w 6.9 Racha thrust earthquake (M_s=7.0) occurred on April 29, 1991 at 09:12:48.1 GMT along the southern slope of the eastern end of the western Greater Caucasus Mountains where the Greater Caucasus overthrust the Dzirula Massif (see Figure 2.1). The event can be divided into four distinct subevents with a total duration of 22 seconds (*Fuenzalida et al*, 1997). The rupture area is located in the Gagra-Dzhava thrust sheet of Jurassic sedimentary rocks which is located about 40 km southwest of the main thrust of the Greater Caucasus. This is about 120 km north of Tbilisi in the Republic of Georgia and partly in the district of Southern Ossetia. No surface rupture was observed, though there were large landslides, new groundwater sources, and cracks on top of anticlines (*Fuenzalida et al*, 1997). Triep et al (1995) proposed two possible fault surfaces: 1) a contact between crystalline basement of the Dzirula Massif below and the Jurassic Gagra-Dzhava thrust sheet complex above or 2) a fault contained en-

tirely within the Dzirula Massif.

Different research groups have reported different earthquake parameters. Those of Fuenzalida et al (1997), Tan (2005), Triep et al (1995), the Harvard Centroid Moment Tensor (CMT) catalog, and the National Earthquake Information Center (NEIC) are summarized in Table 3.1. Total coseismic moment, mainshock-only moment, and errors are indicated where available. The moment for NEIC was calculated from their reported magnitude, M_s = 7.30, using the relation:

$$\log M_0 = 1.5M_s + 16.1 \tag{3.1}$$

RACHA SOURCE PARAMETERS

Group	Strike	Dip	Rake	Depth (km)	Moment (N m)	Lat, Lon
Fuenzalida	286.7	29	92.4	4.81	3.146×10^{19}	42.42°N
et al	±1.3°	±0.6°	±1.2°	±0.2	(2.27×10^{19})	43.69°E
Tan	287°	30°	90°	6	3.195×10^{19} (1.952×10^{19})	42.42°N 43.67°E
Triep	292.9	24	97.7	4.42	n/a	42.4238°N
et al	±6.2°	±2.9°	±7.4°	±2.1	(2.25×10^{19})	43.6643°E
Harvard CMT	288°	39°	106°	22.3	3.34×10^{19} (n/a)	42.60°N 43.61°E
NEIC	n/a	n/a	n/a	17	1.12×10^{20} (n/a)	42.453°N 43.673°E

Table 3.1: Racha source parameters according to different sources. Moment is listed with total coseismic moment above and mainshock-only moment below in parentheses.

Among Fuenzalida et al (1997), Tan (2005), and Triep et al (1995) the total

coseismic moments reported are similar as are the mainshock-only moments. All three groups of researchers obtained their results through inversion of teleseismic body waves. The Harvard CMT and, to a much greater extent, the NEIC reported magnitudes are larger than those of the aforementioned studies. The hypocentral depths of these latter two sources are also significantly deeper. These differences may arise due to the Harvard CMT method being being based on longer period waves (free oscillations) and the NEIC result having larger uncertainties due to it being a preliminary estimate that has not necessarily been thoroughly analyzed.

Chapter 4

Postseismic Deformation Processes

Postseismic deformation of the earth's surface shows the earth's time-dependent response to a step stress change induced by an earthquake. Modeling postseismic deformation can help place constraints on the rheology and structure of the crust and upper mantle in the vicinity of the earthquake (e.g. *Freed et al*, 2006; *Hearn et al*, 2002).

Postseismic deformation resulting from a shallow crustal earthquake can be observed on a time scale of months to decades and often occurs in a different sense to that of the background motions driving the long-term deformation. This postseismic deformation is typically described by one of two main processes: fault afterslip or viscoelastic relaxation. It is possible for both processes to be responsible for observed deformation, though afterslip usually occurs in the immediate months to years following an earthquake while the effects of viscoelastic relaxation can last for decades (*Pollitz*, 1997).

4.1 Fault Afterslip

Fault afterslip is the accelerated motion that is often observed on the surface of the earth immediately following a large earthquake. This is detected through some means of geodetic measurement, almost exclusively nowadays by the Global Positioning System (GPS). Afterslip can occur up to several years following an earthquake and decays logarithmically with time for one-dimensional models (*Marone et al*, 1991). It is usually observed to occur in areas adjacent to the coseismic rupture.

The generally agreed upon explanation of fault afterslip centers on the principle of rate and state variable friction (*Dietrich*, 1979; *Ruina*, 1983) which explains the varying friction on a fault associated with coseismic and postseismic slip. This posits that friction along an interface is dependent on the speed at which the surfaces slide past each other as well as the state of the interface, which can be considered to be the average age of contacts on the surface (*Dietrich*, 1979):

$$\mu \equiv \mu(V, \theta) = \mu_0 + a \ln(V/V_0) + b \ln(V_0\theta/D_c) \tag{4.1}$$

where V_0 is a reference velocity and D_c is the critical distance over which the surface must move to establish a new set of uncorrelated contacts. In a tectonic setting V_0 is the preseismic creep rate and is less than the long-term plate velocity on a fault that regularly experiences earthquakes. The state variable θ is defined

as

$$\theta = D_c/V \tag{4.2}$$

If θ is set to D_c/V_0 in Equation 4.1, then μ is equal to simply μ_0, that is, the friction at some reference velocity, V_0. Otherwise, plugging Equation 4.2 for θ into Equation 4.1 yields an equation for friction at a steady-state velocity, V (different from the reference velocity V_0):

$$\mu_{ss} = \mu_0 + (a - b)\ln(V/V_0) \tag{4.3}$$

Here the sign of $(a - b)$ determines if the friction becomes less than the background friction, μ_0, (velocity weakening) or greater than μ_0 (velocity strengthening). The quantities a and b are determined experimentally with a representing the observed increase in friction due to a sudden increase in sliding velocity, known as the direct effect, and b representing the decrease in friction from this peak to a stable level (see Figure 4.1).

This means, for example, that a fault patch in a velocity weakening zone will experience a decrease in friction during the slip of an earthquake and will then itself be more likely to fail. For this reason earthquakes can nucleate only in zones of velocity weakening. Velocity strengthening, on the other hand, means that friction will rise during increased slip so that the rupture of an earthquake dies off in a velocity strengthening zone as the increased friction makes this zone only less likely to slip. The means, however, that a velocity strengthening

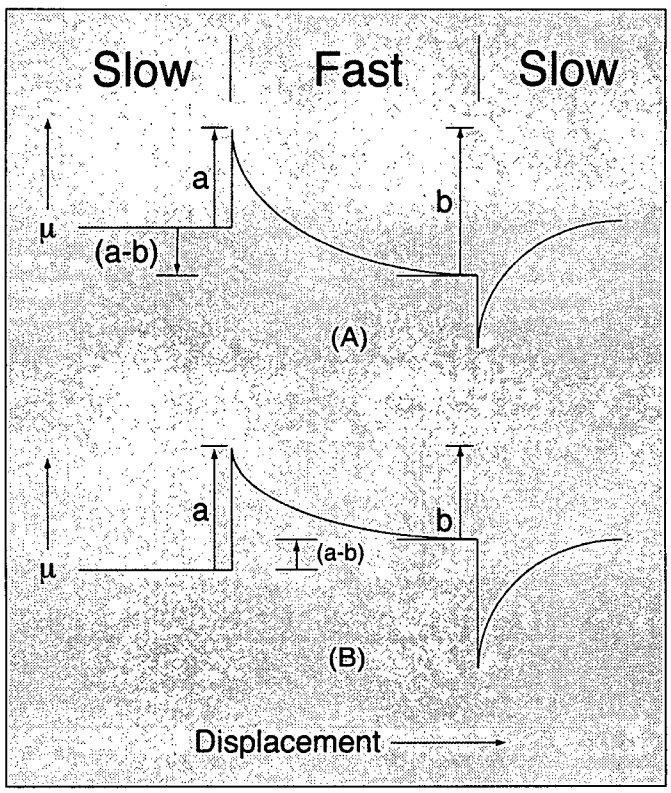

Figure 4.1: Rate and state friction. Friction, μ, is represented in the vertical direction and displacement in the horizontal direction. a is the increase in friction due to a sudden acceleration, and b is the decrease from this peak by the end of the period of greater speed. $a-b$ determines if a medium experiences (a) velocity weakening (negative) or (b) velocity strengthening (positive).

zone absorbs some of these earthquake stresses which must be then dissipated by enhanced creep (as opposed to sudden failure) along the fault. This is afterslip.

The uppermost layer of the crust is a velocity strengthening zone. Its depth can extend down to several kilometers, and it is usually associated with an area of fault gouge and/or unconsolidated sediments (*Marone et al*, 1991). The boundary between velocity strengthening and velocity weakening can be inferred from the cutoff depth of aftershocks. Above this cutoff depth, postseismic stresses are relieved not by aftershocks but rather by afterslip.

Beneath the seismogenic zone (generally 3-12 km depth) is also an area of velocity strengthening friction. Tse and Rice (1986) showed that the onset of this lower zone can be explained by the geothermal gradient. That is, at temperatures at and above 300°C the frictional regime of an average granite sample changes from velocity weakening to velocity strengthening. As well, modeling confirms that postseismic motion at this depth can be regarded as deep afterslip or viscous shear zone creep along a discrete surface as it is not necessary to model a broad region of deformation to achieve a valid result. Blanpied et al (1991) built on these results by including the effect of fluid pressure and concluded that velocity weakening exists at a temperature range of 100°-350°C for a similar granite sample.

Even though much of the stress drop during an earthquake occurs in the velocity-weakening zone, the overlying velocity-strengthening zone will also experience displacement as the two are coupled together. The amount of displacement experienced at the surface (velocity-strengthening zone) can be likened

to a spring whose stiffness controls how much coseismic slip from the velocity-weakening zone is absorbed and how much is transmitted to the surface (*Marone et al*, 1991). If the spring is very stiff, the coseismic slip at the surface will be almost equal to that at the base of the velocity-strengthening zone. Conversely, in a very weak spring almost no coseismic slip will be experienced at the surface. In either case afterslip can be expected with sufficient time to make up the difference between coseismic slip at the surface and coseismic slip at the base of the velocity-strengthening zone. This is, of course, assuming no plastic deformation of rock surrounding the fault.

In their afterslip model, Marone et al (1991) calculated the stiffness of the velocity-strengthening zone as the ratio of the shear modulus to this layer's thickness. The means then that a thinner velocity-strengthening layer translates to a higher stiffness that will mean that most of the surface displacement will be the result of coseismic slip rather than afterslip.

4.2 Viscoelastic Relaxation

In the context of this study viscoelastic relaxation refers to the time-dependent response of a viscoelastic layer in the lower crust or upper mantle to the stresses induced in it by a shallow earthquake in an overriding elastic layer. A viscoelastic material responds elastically on short time scales and viscously on long time scales. In a perfectly elastic earth, any elastic response on the surface would occur almost immediately, while in an earth with a viscoelastic layer there is an

initial elastic response followed by transient deformation generally governed by the viscosity, thickness, and depth of the viscoelastic layer (*Elasser*, 1969; *Nur and Mavko*, 1974). The basic idea of delayed deformation following an increase in stress is similar to that with fault afterslip.

There are a few different types of linear viscoelastic rheologies including Maxwell, standard linear solid, and Burgers Body. Maxwell rheology followed by the standard linear solid rheology are the most commonly used in crustal deformation modeling (*Hetland and Hager*, 2005). A Maxwell rheology is what is used in this study, and its fundamental rheological law relating strain rate ($d\epsilon/dt$), stress (σ), and rate of change of stress ($d\sigma/dt$) in a one-dimensional form is (*Turcotte and Schubert*, 2002):

$$\frac{d\epsilon}{dt} = \frac{1}{2\eta}\sigma + \frac{1}{E}\frac{d\sigma}{dt} \tag{4.4}$$

where η is viscosity and E is Young's modulus.

The other linear rheologies differ in that they have either a yield strength (standard linear solid) or two characteristic viscosities (Burgers Body). In non-linear rheologies, which are not considered here, viscosity depends on the differential stress.

The viscoelastic layer, or that which is most capable of ductile deformation, is typically taken to be the asthenosphere (*Elasser*, 1969), and early models focused only on an elastic layer (upper crust) overlying a viscoelastic half-space

(e.g. *Nur and Mavko*, 1974). Subsequent models have included a viscoelastic layer positioned between two other elastic layers, for example, a viscoelastic lower crust situated between an elastic upper crust and an elastic upper mantle. Rather than having a homogenous viscosity some studies have modeled a depth-varying viscosity (e.g. *Pollitz et al*, 2000; *Freed et al*, 2006).

The general method of solution of the viscoelastic response to the stresses induced by an earthquake are to first find the static displacements and stresses in an entirely elastic half-space. The correspondence principle (*Fung*, 1965) and the Laplace transform are then used to find the temporal response to these stresses (*Nur and Mavko*, 1974). Use of the correspondence principle allows results from linear elasticity to be transformed to equivalent results for a Maxwell material through use of the properties of the Fourier transform.

4.3 Other Postseismic Processes

Other possible postseismic deformation mechanisms include shallow crustal anelastic deformation (e.g. folding of weak sediments) and poroelastic rebound which refers to a reorganization of crustal fluids due to a stress regime change caused by an earthquake. Anelastic deformation can be modeled as afterslip along a plane with afterslip acting as a proxy for such deformation (*Donnellan and Lyzenga*, 1998). It has been shown that poroelastic deformation, where it exists, tends to counteract the vertical postseismic effects of afterslip by inducing a component of subsidence in regions of positive coseismic stress change (compression) and

uplift in regions of negative stress change (extension) (*Peltzer et al*, 1996; *Peltzer et al*, 1998) where the opposite directions of motion would be expected in the near field from afterslip. A much smaller amount of horizontal motion can be expected to result and is in the direction from tensional to compressional coseismic stress change. Peltzer et al (1996, 1998) were able to simulate this effect by lowering Poisson's ratio by 0.03 to represent the change between undrained (coseismic) and drained (postseismic) crustal material.

Poisson's ratio, ν, represents the compressibility of a material with the (at least theoretical) range of values being 0-0.5 with increasing ν corresponding to decreasing compressibility. For a uniaxial stress in the 1-direction, Poisson's ratio is defined as:

$$\epsilon_2 = \epsilon_3 = -\nu\epsilon_1 \tag{4.5}$$

with the ϵ terms being normal strain.

To see why the range of Poisson's ratio is 0-0.5, consider the dilation, Δ, of a volume:

$$\Delta = \epsilon_1 + \epsilon_2 + \epsilon_3 = \epsilon_1(1 - 2\nu) \tag{4.6}$$

For a totally compressible material, ν must equal zero so that dilation is represented entirely by the strain in the 1-direction. Alternatively, ν must equal 0.5

for the dilational to equal 0, an incompressible material.

Chapter 5

Other Postseismic Deformation Studies

There are a few other examples of GPS postseismic deformation studies of continental thrust earthquakes (similar to the Racha earthquake). Consideration of these results helps put those of this study into perspective. Postseismic deformation studies of other types of earthquakes are also mentioned below in order to demonstrate the types of results typically found.

Continental Thrust Earthquakes

Chi-Chi, Taiwan

An event with very similar parameters to the Racha earthquake (except magnitude) is the September 21, 1999 Chi-Chi, Taiwan earthquake (M_w=7.6). It had a hypocenter depth of 8 km, dip of 30°, and rake of 85°(*Chang et al*, 2000). The

primary process responsible for the first three months of postseismic deformation was found to be fault afterslip with the majority of afterslip occurring where coseismic slip was minimal (*Hsu et al*, 2002).

The afterslip during the first 3 months after the earthquake is equivalent to about 7% of the coseismic moment (*Hsu et al*, 2002), and the first 15 months constitute about 16% with this equaling 2.3 times the aftershock moment (aftershock moment = 43% of afterslip moment) (*Yu et al*, 2003). That is, the first 3 months make up about 44% of the afterslip of the first 15 months. This highlights that afterslip starts soon after the earthquake and decays with time.

It has also been shown that a combination of afterslip and viscoelastic models can explain GPS measurements in the first few months after the earthquake with afterslip being dominant around the rupture zone and viscoelastic relaxation away from this zone (*Sheu and Shieh*, 2004). A lower-crustal viscosity of 5×10^{17} Pa s (determined from laboratory measurements) and the long-term strain rate were found to best fit GPS data from far-field sites. Preseismic GPS data in Taiwan have also been modeled showing that a viscoelastic asthenosphere below 27-39 km depth with a viscosity of $0.5 - 4 \times 10^{19}$ Pa s best fits the data (*Johnson et al*, 2005).

Northridge, California

The January 17, 1994 Northridge earthquake (M_w=6.7) had a hypocentral depth of 20 km. In their two-year postseismic deformation study, Donnellan and Lyzenga (1998) found that most postseismic deformation occurred within the

first year following the earthquake and that fault afterslip was the dominant process, at least for the first few years. Their modeled two-year afterslip is equal to 22% of the coseismic moment, and of this afterslip only 10% could be accounted for with aftershocks. Only sites closer to the rupture area were found to show a clear non-linear postseismic trend (*Donnellan and Lyzenga*, 1998).

Loma Prieta, California

The October 17, 1989 M_w=6.9 Loma Prieta earthquake occurred on a buried 70°-dipping fault (*Dietz and Ellsworth*, 1990). Shallow afterslip on the coseismic thrust as well as on an adjacent thrust was found to be the dominant postseismic process and was active for about 5 years following the quake (*Segall et al*, 2000). The moment released by this afterslip was equivalent to about 10% of the coseismic moment. Bürgmann et al (1997) also found that afterslip and not viscoelastic relaxation was responsible for the first 5 years of postseismic geodetic observations and accounted for several orders of magnitude more moment release than that of aftershocks. GPS site velocities were accelerated over background levels only within 20 km of the earthquake rupture.

Non-Thrust Continental Earthquakes

The strike-slip August 17, 1999 M_w=7.5 Izmit, Turkey earthquake exhibited afterslip in the immediate 87-day postseismic time period equal to about 20% of the coseismic moment (*Bürgmann et al*, 2002). Of this, only 5% of the moment could be attributed to aftershocks (*Reilinger et al*, 2000).

The first two years of postseismic deformation following the 2002 strike-slip M_w=7.9 Denali, Alaska earthquake have been modeled simultaneously with a combination of deformation mechanisms using 41 GPS sites (*Freed et al*, 2006). Far-field GPS sites were best explained with a viscoelastic upper mantle (3×10^{18} Pa s). Shallow and deep afterslip were better fit to nearer GPS sites. Finally, poroelastic rebound was seen to be active in the immediate area around the fault rupture.

Early postseismic deformation following the 1992 strike-slip M_w=7.3 Landers, California earthquake had been modeled with viscoelastic relaxation of the upper mantle ($8 \pm 4 \times 10^{18}$ Pa s) (*Pollitz et al*, 2000), a viscoelastic upper mantle of 10^{17} Pa s (*Yu et al*, 1996), and a viscoelastic lower crust of 10^{18} Pa s (*Deng et al*, 1998). It has since been shown that these low viscosities in the lower-crust or upper-mantle do not fit later GPS measurements well as they predict deformation rates that are much too large. Deep afterslip (*Savage and Svarc*, 1997) a combination of deep afterslip and poroelastic rebound (*Peltzer et al*, 1998; *Fialko*, 2004), or a non-linear (power-law) viscoelastic lower or upper mantle (*Freed and Bürgmann*, 2004) are now considered to be mechanisms more likely responsible for the postseismic deformation of Landers.

Five months of postseismic deformation of the 1999 strike-slip M_w=7.1 Hector Mine, California earthquake have been modeled with deep afterslip using an elastic half-space (*Owen et al*, 2002). The first three years of postseismic deformation were found to be best modeled with a non-linear (power-law) viscoelastic upper mantle.

Chapter 6

GPS Data

The data used to constrain the models in this study are Global Positioning System (GPS) position measurements. The technique of using GPS satellites for millimeter-scale geodetic measurements had its beginnings around the start of the 1980s (*Dixon*, 1991). Triangulation with at least three GPS satellites can determine position of a receiver on the ground with an accuracy to about one meter. This is achieved my measuring the time it takes for a signal from the satellite to reach the receiver and by taking into account satellite and receiver clock errors and well as atmospheric effects. Finer scale precision is obtained using relative positioning to the global network of fixed stations of the International GNSS Service (IGS) that are spread about a few hundred kilometers apart from each other. (GNSS stands for Global Navigation Satellite System.)

6.1 Stations and Time Points

There were a total of eight GPS sites in and around the Racha rupture area (see Figure 6.1) that were measured at some or all of the following time points: 1991.56301, 1994.76575, 1996.73907, 1998.71096, and 2000.75819. The first time point, 1991.56301, is July 23, 1991, 2 months and 24 days after the Racha earthquake. This is a relatively small amount of data when compared with other postseismic deformation studies. Table 6.1 highlights this by showing the study duration, number of GPS stations, and data points per station for several other studies.

STUDY	STUDY DURATION	NUM. GPS STATIONS	AVG. OBS. PER STATION
Chi-Chi (*Yu et al*, 2003)	15 months	80	7
Denali (*Freed et al*, 2006)	2 years	41	(daily)
Hector Mine (*Owen et al*, 2002)	5 months	32	20
Izmit (*Bürgmann et al*, 2002)	87 days	47	27
Loma Prieta (*Bürgmann et al*, 1997)	5 years	50	14
Loma Prieta (*Segall et al*, 2000)	8.5 years	62	18
Northridge (*Donnellan and Lyzenga*, 1998)	2 years	8	5

Table 6.1: Study duration, number of GPS stations, and average number of observations of other postseismic deformation studies.

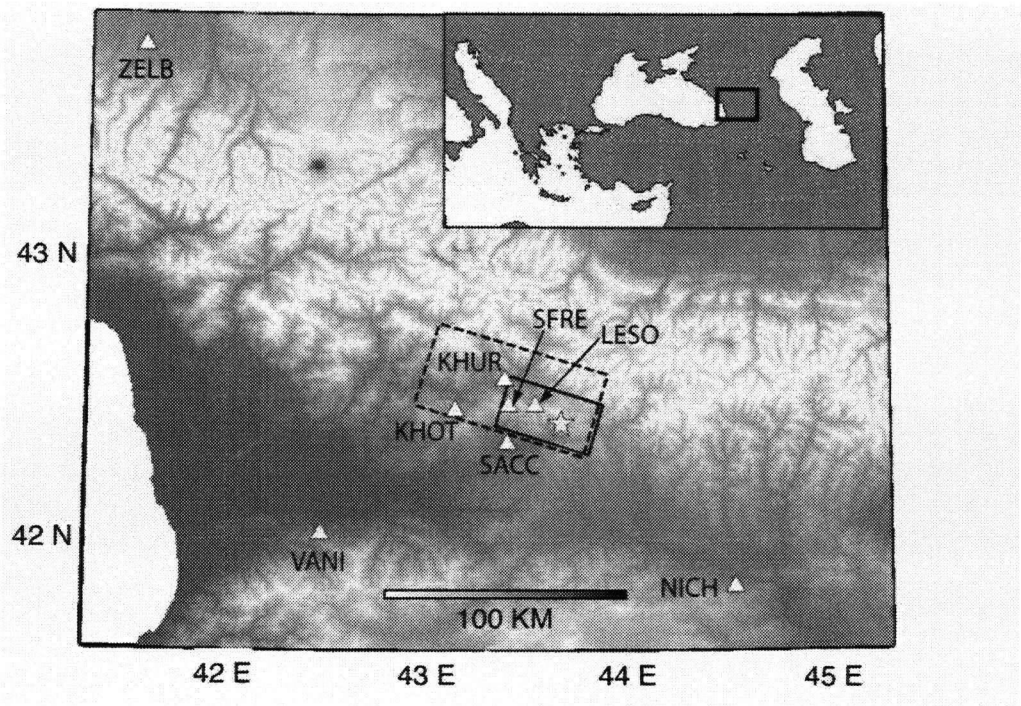

Figure 6.1: Location of GPS sites (triangles). Solid rectangle indicates the modeled coseismic slip plane and star the epicenter of Tan (2005), and dashed plane indicates rectangle of afterslip plane.

6.2 Acquisition

The GPS measurements were obtained during surveys conducted by Rob Reilinger of MIT along with associates from MIT, Indiana University, and in Russia and Armenia (*Reilinger et al*, 1997) which lasted for about two weeks around the time of each reported measurement. The stations were observed for about 8-12 hours per day for the 1991 measurement and for 10-24 hours per day for subsequent measurements.

6.3 Analysis

The GPS data were analyzed by Simon McClusky of MIT using the GAMIT/ GLOBK software (*King and Bock*, 2004) in two steps. The first was to estimate station coordinates, satellite orbital parameters, atmospheric delay corrections, and earth orientation parameters for each observation session using GPS pseudoranges and phases. All parameter estimates were loosely constrained. The second step was to combine parameter estimates and covariances from all sessions and apply International Terrestrial Reference Frame (ITRF) position and velocity constraints using 14 global IGS core sites (*Reilinger et al*, 1997).

6.4 Position Measurements

Appendix A shows the GPS site position measurements in the ITRF2000 reference frame. This reference frame is defined by a no net rotation condition applied to approximately 200 base station GPS sites on the earth's surface that allow this reference frame to be free from any plate tectonic motion model (*Altamimi et al*, 2002). This model is further constrained by Very Long Baseline Interferometry (VLBI) and Satellite Laser Ranging (SLR) instrumentation.

Corrections to Sites SACC and ZELB/ZECK

In an effort to make the most of a limited data set, a position value was interpolated for that missing at SACC in 1998. Such an interpolation was considered

reasonable as no significant deformation signal was expected at this stage in the postseismic period (see *Other Postseismic Deformation Studies*). This was done by a simple linear interpolation between the position data for 1996 and 2000. The error given to the 1998 data point was an average of the error from the other four time points. This is somewhat conservative as this results in larger errors for the north and up components than if the average of only 1996 and 2000 were considered, while the error of the east component remains about the same. As it turns out, this interpolation became redundant due to how the data were ultimately used in modeling, explained below.

Stations ZELB and ZECK refer to the same location but with position measurements taken over different time periods (1991-1996 and 1998-2000, respectively). Their reported values reflect different baselines, that is, to different fixed stations in the IGS network. In order to produce one station (called ZELB), the station with later measurements, ZECK, was combined with ZELB to produce one continuous time-series. This was done by first extrapolating the position of ZELB to 1998 by using the 1991-1996 velocity. The error for this time point was assigned that of ZECK in 1998. The measurement assigned to ZELB at 2000 was then found using the displacement of ZECK between 1998 and 2000. The error from ZECK at 2000 was likewise assigned to that of ZELB at 2000.

Conversion from ITRF2000 to Eurasian Reference Frame

It was necessary to apply vectors to each station to convert from the ITRF2000 reference frame to a Eurasian reference frame to thereby allow for a more in-

tuitive consideration of individual vectors. This means that displacement and velocity vectors could now be considered relative to a fixed and nondeforming Eurasian continent (north side of Racha rupture area). Velocities derived by Simon McClusky of MIT from the plate motion model of DeMets et al (1994) to perform this conversion are displayed in Appendix B. These velocities were multiplied by the time lapsed since the first position measurement (1991.56301) and subtracted from the ITRF2000 position measurements to produce new values oriented to a Eurasian reference frame. The first measurement did not need to be adjusted since all subsequent use of the data involved displacements and velocities relative to this first measurement.

6.5 Velocity Decay in GPS Time-Series

Once in the Eurasian reference frame the data were analyzed to see what kind of accelerated postseismic signal, if any, stood out. This would be manifested by a decaying slope on a displacement-time plot whereby postseismic velocities are initially high and then decay to a slower rate of motion later in the postseismic period. A logarithmic time-series decay can be expected to occur as a result of an afterslip process (*Marone et al*, 1991), and an exponential decay will result from viscoelastic relaxation (for near-field GPS sites).

The priority in trying to detect accelerated postseismic motion was to see if any function with a decaying slope could better fit the GPS position data than could a straight line. In this light, exponential and logarithmic functions were

initially tested, but it was decided to use only a logarithmic function as either function provided a similar fit and the logarithmic function was more straightforward to apply. It was then reasoned that if the residuals of the position data to a logarithmic function were less than those to a straight line, that this could be indicative of accelerated postseismic motion, due either to afterslip or viscoelastic relaxation.

The form of the logarithmic function fit to the data is:

$$x(t) = x_0 + v(t - t_m) + [C + \lambda \ln(1 + (t - t_{eq}/\tau))]\Theta(t_{eq}) \quad (6.1)$$

where v is long-term velocity, C is coseismic offset, λ is the amplitude of the logarithmic term, τ is the time constant of the logarithmic function, $\Theta(t_{eq})$ is a Heavy-side step function at the time of the earthquake (t_{eq}), and t_m is the first time of the time-series.

An application developed by Thomas Herring and Simon McClusky of MIT (Tsview) facilitates the fitting of this logarithmic function. It estimates values of the amplitude, λ, and long-term velocity, v, and allows the start time of the earthquake, t_{eq}, and the time constant, τ, to be adjusted. t_{eq} was set to 1991.32434 (corresponding to 9:12:48.1 GMT on April 29, 1991), and τ was given a typical value of 10 years (*McClusky*, personal comm.). To test the influence of the choice of τ on the fit to data, values between 1 and 100 were used with essentially no difference in fit found.

Residuals to the linear and logarithmic fits were calculated using weighted standard deviation (WSTD):

$$\text{WSTD} = \sqrt{\frac{\frac{1}{N'-1}\sum_{i=1}^{N} w_i(x_i - \bar{x}_w)^2}{\frac{1}{N'}\sum_{i=1}^{N} w_i}} \tag{6.2}$$

where w_i is the weight for the ith observation (in this case the inverse of the 1-σ error), N' is the number of non-zero weights, and $\bar{x}_w$ is the weighted mean of the observations:

$$\bar{x}_w = \frac{\sum_{i=1}^{N} w_i x_i}{\sum_{i=1}^{N} w_i} \tag{6.3}$$

The WSTD is essentially a regular standard deviation with greater emphasis or weight placed on those observations that are better determined (that have smaller errors).

The calculated residuals are shown in Table 6.2. It can be seen here that sites KHUR (N), LESO (N, E, U), SACC (E), and ZELB (E, U) show improvements in the fit of their position data to a logarithmic function versus a linear fit. KHUR, LESO, and SACC are located in the immediate earthquake rupture area, and therefore their results are considered a potential indication of accelerated postseismic deformation. As ZELB is located far from the rupture area on the other side of the Greater Caucasus Mountains and had relatively small

displacements, it was not viewed to be as significant.

Station	Dir.	Linear Model		Logarithmic Model		
		WSTD	Linear Rate	WSTD	Linear Rate	Amplitude
KHOT	N	5.16	0.22 ± 1.07	6.32	-1.08 ± 2.59	5.17 ± 8.96
	E	4.29	2.57 ± 1.09	5.66	0.96 ± 4.42	8.37 ± 21.66
	U	16.31	2.50 ± 3.54	19.67	-1.93 ± 8.40	18.28 ± 29.86
KHUR	N	4.19	-2.42 ± 1.02	2.82	-0.36 ± 1.31	-7.74 ± 4.18
	E	3.24	0.83 ± 0.92	3.94	-0.28 ± 2.18	4.32 ± 7.27
	U	14.49	2.55 ± 3.80	14.94	-3.32 ± 7.37	23.71 ± 25.24
LESO	N	4.92	-2.36 ± 1.40	0.75	-0.14 ± 0.88	-7.06 ± 2.43
	E	4.98	2.54 ± 1.43	0.85	3.76 ± 1.01	-4.80 ± 3.45
	U	22.83	4.17 ± 7.21	3.74	-6.96 ± 4.75	41.59 ± 15.40
NICH	N	0.67	-0.48 ± 0.55	0.67	-1.71 ± 1.17	2.76 ± 2.32
	E	0.87	1.60 ± 0.68	0.87	6.51 ± 1.52	-10.22 ± 2.83
	U	3.18	2.13 ± 3.25	3.18	-15.56 ± 6.28	53.46 ± 16.25
SACC	N	0.31	2.18 ± 0.06	1.00	2.09 ± 0.90	0.23 ± 2.08
	E	6.63	2.84 ± 2.15	1.14	2.81 ± 1.53	0.09 ± 3.53
	U	12.46	5.61 ± 3.22	5.07	3.88 ± 4.84	5.84 ± 13.70
SFRE	N	3.90	0.25 ± 0.77	3.88	1.68 ± 1.61	-1.61 ± 8.52
	E	3.62	0.41 ± 0.86	4.35	1.51 ± 2.05	7.06 ± 3.75
	U	20.55	8.66 ± 4.24	19.79	0.92 ± 8.27	-35.01 ± 29.85
VANI	N	1.57	-0.04 ± 0.39	0.76	-0.64 ± 0.85	1.58 ± 1.98
	E	3.68	3.04 ± 1.01	0.83	2.51 ± 0.99	1.40 ± 2.32
	U	26.48	0.33 ± 7.88	4.32	-2.21 ± 5.17	8.68 ± 15.28
ZELB	N	0.24	-0.45 ± 0.09	0.24	-0.52 ± 0.33	-332.69 ± 1.09
	E	4.42	0.50 ± 1.66	0.35	-0.80 ± 0.49	1336 ± 1.51
	U	7.42	-0.12 ± 3.24	0.85	-2.55 ± 1.56	999.36 ± 4.27

Table 6.2: Residuals (WSTD) and linear rates from linear and logarithmic functions fit to data. Amplitude of logarithmic function is also included. All values are in mm or mm/yr.

6.6 Secular Correction

Typically when conducting a postseismic study GPS data are available from before the earthquake, and these allow for an estimation of interseismic, or secular, tectonic motion. This information can be used to calculate constant preseismic velocities that are used to correct the postseismic displacement time series. In so doing the postseismic signal is isolated. Unfortunately in the case of this study, no such preseismic data are available, forcing the search for another method to estimate the secular deformation. Two such methods were explored, using data from late in the time-series and using estimates from a regional tectonic block model.

Secular Correction from Time-Series

One possibility is to use the latter portion of the time-series as an approximation of the secular tectonic signal, that is, to assume that all or most postseismic deformation was completed by this time. This has the advantage of being able to use data from the same GPS stations, and so if the assumption of completed postseismic deformation is accurate it is potentially nearly as good as having a preseismic data set from these stations. This method of course precludes the possibility of testing for postseismic deformation late in the time-series. As explained in the section on other postseismic deformation studies, afterslip was found to be almost exclusively responsible for observed postseismic deformation in continental thrust earthquakes, and this afterslip was found to last for no

longer than five years.

In considering the Racha data set for a secular deformation estimation, the two possibilities were to use the 1998-2000 measurements or those from 1996-2000. The latter was adopted as this allowed for more data to be used thereby allowing for a more reliable fit. It also made it possible to use two more sites in the analysis (LESO and VANI) by allowing a line to be fit to two of the three time points (1996.73907, 1998.71096, 2000.75819) if only two data points were available. By starting at 1996 to estimate the secular tectonic signal, there is a five-year gap to the earthquake, consistent with findings at Loma Prieta (an earthquake of the same magnitude as Racha) that all afterslip was finished after five years (*Segall et al*, 2000). Once the 1996-2000 velocities for each site were calculated, they were multiplied by either the 1991-1994 or 1994-1996 time period and then subtracted from either set of respective displacements. This method is hereafter referred to as Time-Series Correction (TSC).

Secular Correction from Tectonic Block Model

An alternative method to removing the secular tectonic signal from the time-series is to use horizontal velocities (no vertical velocities are available) predicted by a kinematic block model of the Africa-Arabia-Eurasia region (*Reilinger et al*, 2006). (A kinematic model is one whose motions are valid spatially without regard for the processes responsible.) This model is comprised of large blocks representing coherent, undeforming tectonic units based on a best fit to GPS velocities from 1988 to 2005. In this model the blocks are separated by

faults slipping at a prescribed rate below a "locking depth" of 15 km.

A locking depth refers to the thickness at the top of the crust which is modeled as not slipping interseismically. In at least a strike-slip fault situation the breadth of deformation perpendicular to the fault is proportional to the arctan of the locking depth (*Savage and Burford*, 1973). That is, a thicker locked surface layer means that strain will be manifested in a broader zone around the fault:

$$y \alpha \arctan\left(\frac{x}{D}\right) \tag{6.4}$$

where y is displacement at a surface point, x is perpendicular distance from the fault, and D is locking depth.

The boundary along two of the blocks in this model is a straight line passing through the Main Caucasus Thrust (MCT) representing the boundary between the Eurasian and Black Sea and Azerbaijan blocks (see Figure 6.2). As the MCT is actually north of the Racha rupture area, Philip Vernant of MIT was able to adjust this model to have the "MCT" pass through the Racha rupture area, with the site SACC on one side and the other near-field sites KHOT, KHUR, LESO, and SFRE on the other (see Figure 6.1).

The temporal range of data used for this block model encapsulates and averages the pre-, co-, and early postseismic deformation of the Racha earthquake. As such, it may overestimate preseismic velocities due to the expectation that coseismic and early postseismic velocities are much larger than preseismic ones.

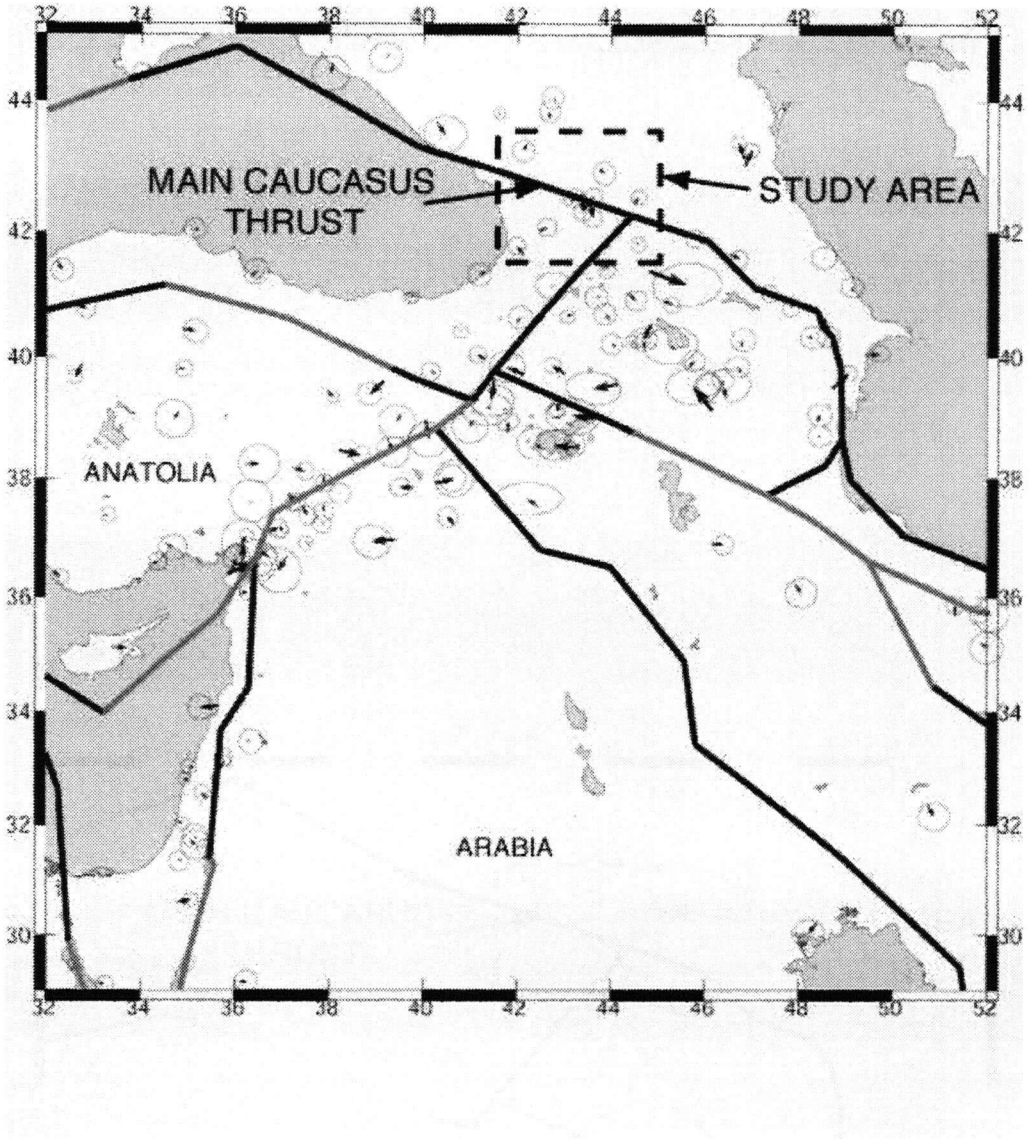

Figure 6.2: Map of part of the tectonic block model used in producing secular velocity estimates (*Reilinger et al*, 2006). The area of this study as well as the straight line estimate of the Main Caucasus Thrust plate boundary are indicated.

Also, the large scale nature of this model does not necessarily lend itself well to accurate deformation predictions on the scale of the Racha GPS network. For example, the model contains one fault in the Caucasus (through the Racha rupture area) and does not take into account secular motion along other nearby fault structures, most notably the actual MCT to the north. Finally, there is no vertical component in the model, and so one-third of the GPS data are not being corrected by the use of this model, though the secular vertical signal is expected to be small. Though unable to explain all the complexity contained within, the block model may still be a potentially useful, independent approximation of the background tectonic signal that can be used in the absence of actual site-specific preseismic GPS velocities.

Along the "MCT" the block model calculated a dip-slip (reverse) slip rate of 3.6 ± 0.3 mm/yr and a right lateral strike-slip rate of 0.7 ± 0.2 mm/yr. The site velocities listed in Table 6.3 were calculated using a 10 km locking depth and 30°north-dipping fault surface. Displacements calculated from the block model velocities were then subtracted from the GPS displacements (relative to the first time point, 1991.56301) to try to isolate the postseismic Racha displacements. This method is hereafter referred to as the Block Model Correction (BMC).

Block Model Velocities		
STATION	**North (mm/yr)**	**East (mm/yr)**
KHOT	3.102	0.096
KHUR	1.927	0.114
LESO	2.333	0.059
NICH	6.981	0.650
SACC	3.603	0.398
SFRE	2.524	0.048
VANI	3.874	0.582
ZELB	0.839	0.294

Table 6.3: Block model velocities (mm/yr) used in correcting GPS time-series for secular tectonic displacements.

6.7 Error Combination

Once the data had been corrected for secular deformation by the methods described above the data were differenced to produce displacement (and velocity) values. At this stage, the errors in position at each time point were combined by taking the square root of the sum of the squares of the individual errors.

6.8 Data Used in Modeling

The 1991-1994 period was the primary time period on which postseismic deformation modeling was performed. This is due to it being the earliest period following the Racha event and that most deformation observed following similar earthquakes takes place in the first few years (see Table 6.1). To test this,

GPS displacements from the 1994-1996 period were modeled as well, and data from both time periods are displayed in Appendix C. These data are in the form of displacements (rather than velocities) as there are only the end time points of each period available and all stations share the same exact measurement times. Both the TSC data and BMC data are shown.

Chapter 7

Methods

7.1 Afterslip Inversion Modeling

Afterslip has been modeled kinematically by using the equations describing displacements on the earth's surface due to slip on a fault in an elastic half-space (*Okada*, 1985). The basic form of these equations comes from Steketee (1958):

$$d_i = \frac{1}{F} \iint_{\Sigma} \Delta u_j \left[\lambda \delta_{jk} \frac{\partial d_i^n}{\partial \xi_n} + \mu \left(\frac{\partial d_i^j}{\partial \xi_k} + \frac{\partial d_i^k}{\partial \xi_j} \right) \right] \nu_k d\Sigma \tag{7.1}$$

which describes the surface displacement $d_i\ (x_1, x_2, x_3)$ due to a dislocation $\Delta u_j(\xi_1, \xi_2, \xi_3)$ on a surface, Σ. d_i^j is the ith component of the displacement at (x_1, x_2, x_3) due to the jth direction point force of magnitude F at (ξ_1, ξ_2, ξ_3). δ_{ij} is the Kronecker delta, λ and μ are Lamé constants, ν_k is the direction cosine normal to $d\Sigma$. This assumes uniform slip on rectangular fault patches and is based

on integration of the solution for a point dislocation over the uniform patch.

Okada (1985) expressed Equation 7.1 in terms of strike-slip, dip-slip, and tensile dislocations on a fault surface rather than of a point force. These expressions are integrated to produce displacements on the earth's surface due to slip on a finite rectangular fault patch (*Okada's* equations 25-30, 1985). These are the equations that are typically used for elastic dislocation models and earthquake slip inversions.

To model afterslip a bounded least-squares inversion approach was used (*Stark and Parker*, 1995). In the inversion process, Green's functions, G, are calculated to relate the slip on each fault patch, s_j, to the displacement at each GPS station, d_i in an elastic half-space. The commonly used value of 0.25 was used for Poisson's ratio (e.g. *Hreinsdottir et al*, 2003; *Sheu and Shieh*, 2004).

Tikhonov regularization was used to enforce a smooth slip distribution. This uses a smoothing parameter, β, to facilitate a trade-off between the best fit to data and a smoothly varying solution that is physically plausible. This is achieved by minimizing the terms of misfit and roughness:

$$\|\mathbf{W}^{-1}(\mathbf{G}\vec{s} - \vec{d})\|^2 + \beta^2\|\mathbf{L}\vec{s}\|^2 \tag{7.2}$$

where $\mathbf{W}^T\mathbf{W}$ is the data covariance matrix and $\mathbf{L}$ is the finite difference approximation of the Laplacian operator (∇^2). Multiplying by $\mathbf{W}^{-1}$ weights the misfit term. For example, if a given measurement's error ($\mathbf{W}$) is small, multiplying by $\mathbf{W}^{-1}$ will produce a large value that is relatively more important in the mini-

mization. $||\mathbf{x}||$ means $(\mathbf{x} \cdot \mathbf{x})^{1/2}$ and is necessary to perform in order to have both terms in Equation 7.2 be scalar quantities. Squaring both terms forces both to be positive values.

Afterslip Plane

It is assumed that afterslip occurred on the same plane as the coseismic slip. The coseismic fault plane of Tan (2005) was extended 60 km laterally to each side from the hypocenter, up to the surface, and down to 20 km depth along a 30°slope (120 km × 40 km). Figure 7.1 confirms that this fault plane geometry plots directly through the middle of the aftershock activity (*Fuenzalida et al*, 1997). This not only encloses all of the slip in Tan's 60 km × 24 km coseismic slip model (Figure 7.2) but in the course of testing also captures all slip that the inversion code produced. Tan's fault orientation (Table 3.1) was chosen on the grounds of consistency as this was the only available coseismic slip model and was therefore necessary for the viscoelastic forward-modeling portion of this project. As described subsequently, model results were tested for sensitivity to changes in fault geometry by modifying the fault parameters to match those of some of the other Racha earthquake models and doing separate inversions.

Resolution Testing

In order to determine which areas of the 120 km × 40 km afterslip fault plane the GPS network is able to resolve slip on, a resolution test was conducted. First,

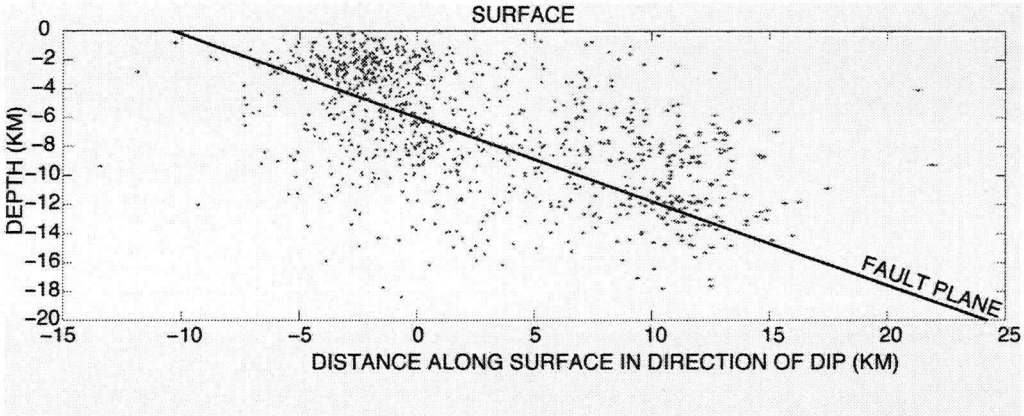

Figure 7.1: Profile perpendicular to strike of afterslip fault plane with geometry of Tan (2005) and two months of aftershocks.

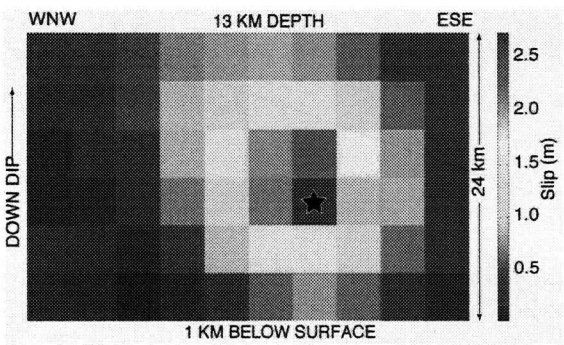

Figure 7.2: Coseismic fault model, from Tan (2005). Displacement is in meters. Each tile is 4 km square.

a "checkerboard" pattern of 20 km × 20 km tiles was constructed with alternating amounts of dip-slip of one or zero meters (Figure 7.3). This was forward-modeled with the resulting GPS displacement vectors then being inverted for slip on the fault plane. If the GPS network is sufficiently dense and evenly distributed around the fault plane, one would expect most of the checkerboard patterned slip to be recovered in the inversion process.

The inversion result in Figure 7.3 demonstrates that the GPS network is capable of constraining slip on only the left (WNW) side of the fault plane. As indicated in the figure only the left 60% of this fault was therefore used for slip inversions. Additionally, the upper-left corner of this section of the fault appears incapable of accurately resolving slip with the given array of GPS sites.

7.2 Viscoelastic Forward Modeling

Viscoelastic postseismic deformation is modeled using the Visco1D code of Pollitz (1992) which solves for displacement on the surface of the earth due to relaxation of viscoelastic layers at depth resulting from an earthquake in an upper elastic layer. The earthquake displacement field is divided into toroidal and spherical components, the equations of static equilibrium are solved for a spherically symmetric 1-D earth model, and (by using a Maxwell rheology) the correspondence principle is used to find the time-dependent solution. The displacement field is calculated using a summation of these normal mode solutions.

This model requires that a finite source as well as elastic and viscoelastic

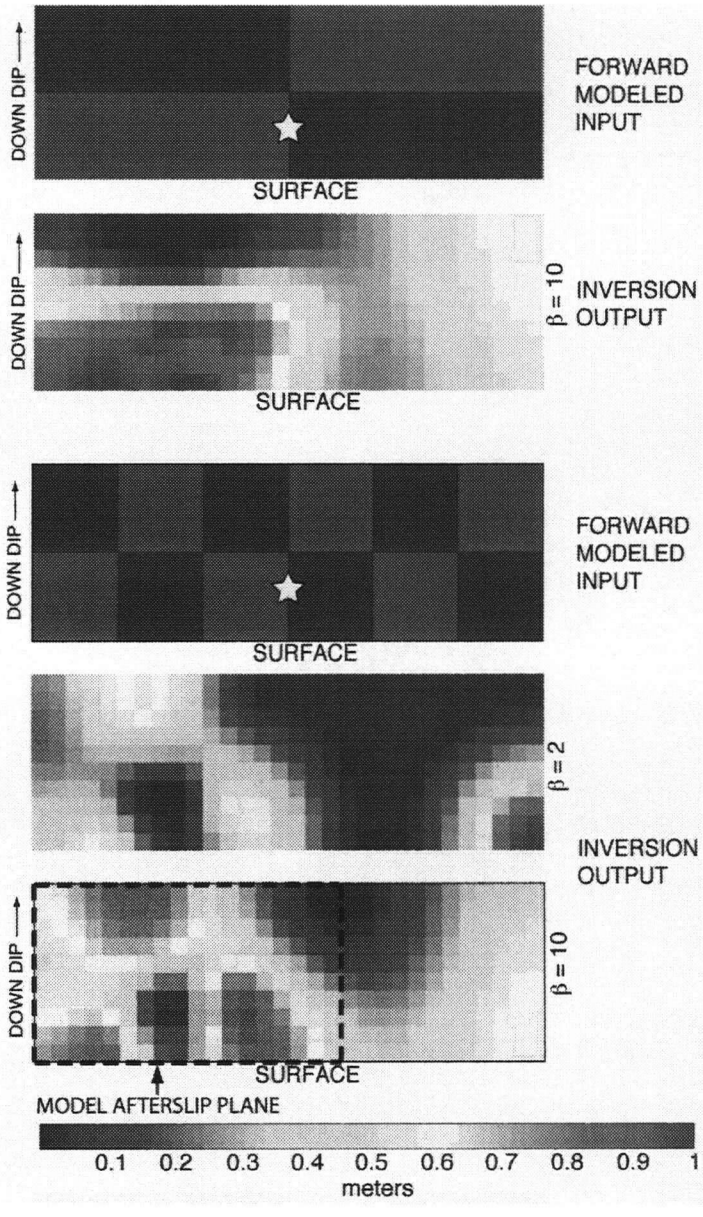

Figure 7.3: Fault plane resolution tests using alternating 1 and 0 meter slip patches on a 120 km × 40 km plane. (a) 60 km × 20 km and (b) 20 km × 20 km sized slip patches were forward modeled (top) and the resulting surface displacement vectors were inverted for slip (bottom) to determine which areas of the modeled fault plane the GPS network can resolve slip on. Inversions were performed using a smoothing, β, of 10 km^2/m except where indicated.

properties of the spherically symmetric layers be specified. With these parameters the code forward models cumulative displacements at prescribed points on the earth's surface, which can then be compared with GPS displacement data. In this model the patterns of displacement are sensitive to the earth model and the earthquake geometry. The viscosity controls the time dependence of the deformation (*Pollitz*, 1992).

Three different viscoelastic lower-crust thicknesses were modeled as was a viscoelastic half-space. A viscoelastic lower-crust is often modeled for post-seismic deformation starting at the cutoff depth of seismicity (e.g. *Pollitz et al*, 2000; *Sheu and Shieh*, 2004). The May and June, 1991 aftershocks found by Fuenzalida et al (1997) do not extend beyond 15 km depth. Therefore, a 30 km thick viscoelastic lower crust (15-45 km depth) was modeled as were also 20 km and 10 km lower crusts (25-45 km depth and 35-45 km depth respectively). Justification for modeling a viscoelastic mantle half-space (45 km and deeper) is the high *Pn* attenuation beneath the Greater Caucasus suggesting little to no mantle lithosphere (*Al-Lazki et al*, 2003).

Earth Model Input File

The Visco1D code requires that an earth model be specified that includes the density (ρ), bulk modulus (K), shear modulus (μ), and viscosity (η) for each spherical layer. Values of the bulk and shear moduli for the crust were obtained using P and S waves obtained by inversion of P and S arrival times from the Racha mainshock and aftershocks (*Triep et al*, 1995) (See Table 2.1). The rela-

tions used for calculating these elastic moduli are:

$$V_p = \sqrt{\frac{\lambda + 2\mu}{\rho}} \tag{7.3}$$

$$V_s = \sqrt{\frac{\mu}{\rho}} \tag{7.4}$$

$$K = \lambda + \frac{2}{3}\mu \tag{7.5}$$

where V_p is the P-wave velocity, V_s is the S-wave velocity, K is the bulk modulus, and λ and μ and the first and second Lamé constants. (μ is also known as the shear modulus.)

Inserting Equation 7.3, Equation 7.5 becomes:

$$K = \rho V_p^2 - \frac{4}{3}\mu \tag{7.6}$$

Equation 7.4 is first used to find the shear modulus (μ). Equation 7.6 is then used to find the bulk modulus (K).

Values for the elastic moduli below the crust as well as density values were obtained using the Preliminary Reference Earth Model (PREM) (*Dziewonski and Anderson*, 1981). It was found, however, that varying values of μ and K below 80 km depth had essentially no effect on the model results, and so in interest of speeding up the model's run time these moduli were assigned constant values below this depth. The values used in the earth model are listed in Appendix D.

Coseismic Slip Model

The slip model input to Visco1D was that of Tan (2005) (Figure 7.2 and Table 7.1). As this slip model represents only the mainshock of the four subevents that together lasted 22 seconds, the Visco1D model displacement results were multiplied by 1.637 which is the ratio of the total moment to mainshock-only moment reported by Tan. This can be done due to the linear relation between stress and strain (Equation 4.4).

COSEISMIC SLIP MODEL VALUES

ALONG STRIKE	**KM DOWN-DIP**					
	0-4	4-8	8-12	12-16	16-20	20-24
ESE	0.109	0.234	0.259	0.238	0.247	0.201
	0.271	0.633	0.869	0.807	0.610	0.366
	0.585	1.325	1.922	1.722	1.120	0.586
	0.778	1.786	2.737	2.378	1.517	0.781
	0.616	1.457	2.172	2.074	1.524	0.869
	0.335	0.884	1.344	1.462	1.265	0.829
	0.140	0.449	0.671	0.847	0.894	0.711
	0.030	0.146	0.209	0.349	0.510	0.500
	0.136	0.188	0.129	0.164	0.323	0.392
WNW	0.149	0.161	0.074	0.088	0.174	0.231

Table 7.1: Coseismic slip on 4 km × 4 km fault patches from model of Tan (2005).

Chapter 8

Results

8.1 Afterslip

1991-1994 Data

The afterslip inversion results from using the 1991-1994 displacements, using the TSC and BMC data and a positivity constraint (no backward slip), are shown in Figure 8.1. Using a smoothing value of 10 km^2/m, the reduction in weighted residual sum of squares (WRSS) relative to a model with zero displacements is 89.7489% for the TSC data and 65.6188% for the BMC data. The amount of afterslip moment estimated by each model is 7.585×10^{18} N m (24% of coseismic moment of Tan (2005)) and 6.015×10^{18} N m (19% of coseismic moment) respectively. It is notable that both secular correction methods produced similar afterslip distributions with the highest concentration of slip occurring along the surface and along strike to the WNW of the coseismic hypocenter. Both models

also show a lobe of afterslip occurring at about 10-16 km depth located about 32 km WNW along strike from the hypocenter. It is also seen in Figure 8.1 through comparison that most of the afterslip occurred immediately adjacent to (and not coincident with) the coseismic slip.

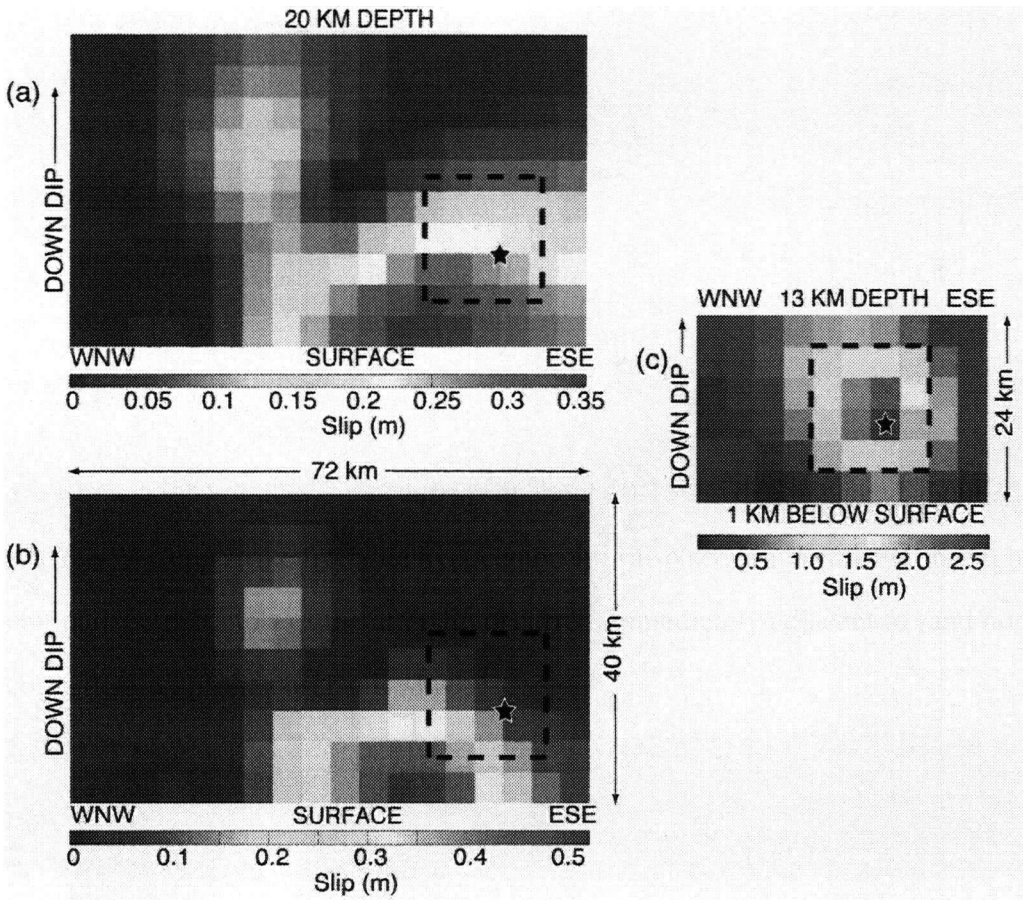

Figure 8.1: 1991-1994 afterslip inversion results using (a) TSC data and (b) BMC data. (c) Coseismic slip model of Tan (2005). Star on each slip plane represents the Racha hypocenter, and each tile is 4 km square. Comparing either afterslip model (a) or (b) with the coseismic slip model (c) shows that the bulk of modeled afterslip occurs away and up-dip from the area of maximum coseismic slip.

To evaluate how well the afterslip models fit the data, modeled afterslip was forward-modeled producing displacement vectors that were compared with the data displacement vectors and 1-σ errors (Figure 8.2). Only the nearest sites to the modeled fault (KHOT, KHUR, LESO, and SFRE) were considered as these show the greatest displacements and therefore are the most affected by fault motions. Model vectors from both TSC and BMC data fit the data of these nearest sites at least just within the 1-σ error ellipses if not almost perfectly.

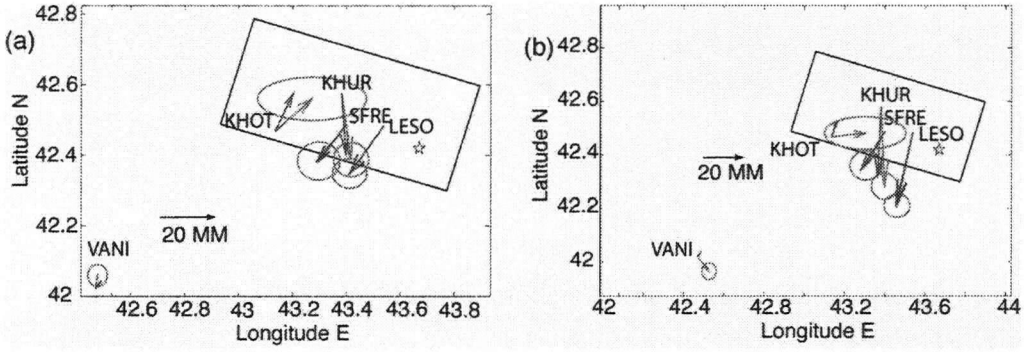

Figure 8.2: Comparison of 1991-1994 data vectors with 1-σ error ellipses (red) with model vectors (blue). Model vectors are produced by forward modeling the afterslip results. (a) is from using TSC data and (b) is from using BMC data. The star represents the Racha epicenter.

Comparison to Data without Secular Correction

To test what effect either of the secular correction methods (TSC or BMC) have on the data set, the 1991-1994 time period was modeled without any secular correction (Figure 8.3). The basic pattern of slip as with the models of secular corrected data is seen along with some additional slip distributed along the edges.

The reduction in WRSS of this model, 51.7435% is less than that of either of the two models based on secular corrected data. The moment of 8.987 $\times 10^{18}$ N m is about 30-40% larger than that of the models with secular correction.

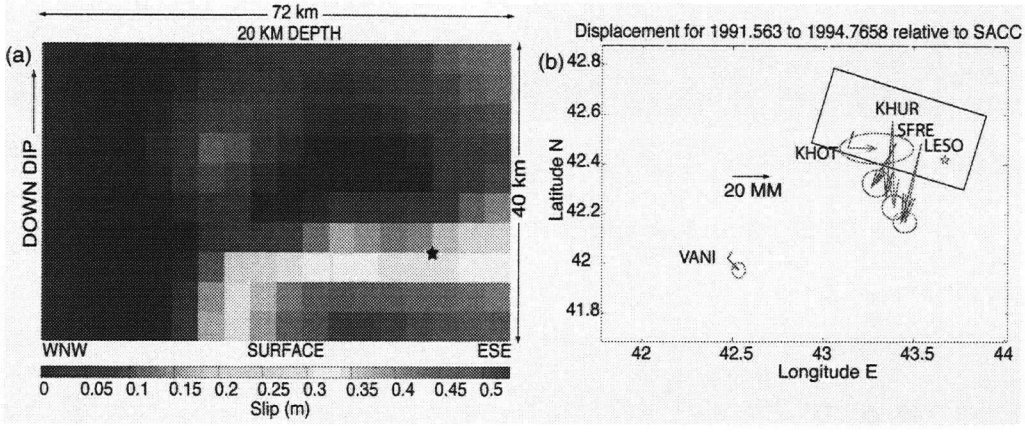

Figure 8.3: 1991-1994 slip inversion using data with no secular correction. WRSS reduction is 51.7435% and the moment is 8.987 $\times 10^{18}$ N m.

To see why the data fitting (WRSS reduction) is significantly worse with the non-secular corrected (NC) data compared to the TSC and BMC data, the data and model vectors of all available sites were plotted for comparison (Figure 8.4). Here it is seen that while all data sets fit the GPS sites close to the fault plane (KHOT, KHUR, LESO, SFRE) reasonably well, it is primarily the more distant sites (NICH, VANI, ZELB) that are fit much less well by NC and to a lesser extent by BMC. (Site NICH is absent from the TSC data due to a lack of data points to establish a 1996-2000 velocity for this site.) Another way of considering this is that the displacement magnitudes of these distant sites in the BMC and NC data are much larger than in the TSC data. The modeled vectors of the distant sites from all three data sets have about the same magnitude.

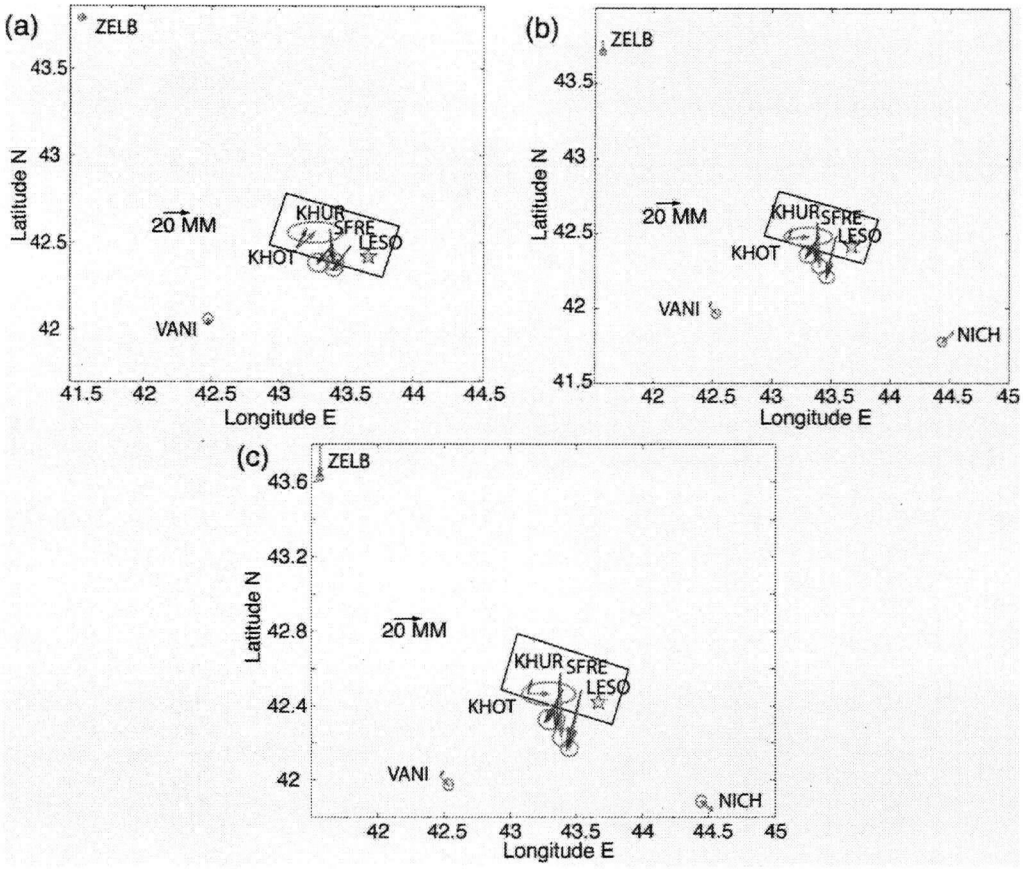

Figure 8.4: 1991-1994 afterslip model and data vectors for all available sites for (a) TSC data (b) BMC data and (c) non-corrected (NC) data.

All Data Sets with Same GPS Sites

The TSC data are lacking the relatively distant site NICH due to the lack of data at this site to determine a 1996-2000 velocity. In the previous section the TSC, BMC, and NC data sets were compared. In order to see what effect NICH has on how well the model fits the BMC and NC data sets, these other data sets were modeled without NICH and the inversion results compared (Figure

8.5). By removing NICH, the BMC model improved its WRSS reduction from 65.6188% to 72.3125%, and the NC model improved slightly from 51.7435% to 53.7368%. The BMC and NC slip models appear almost identical and both of these are very similar to the TSC model.

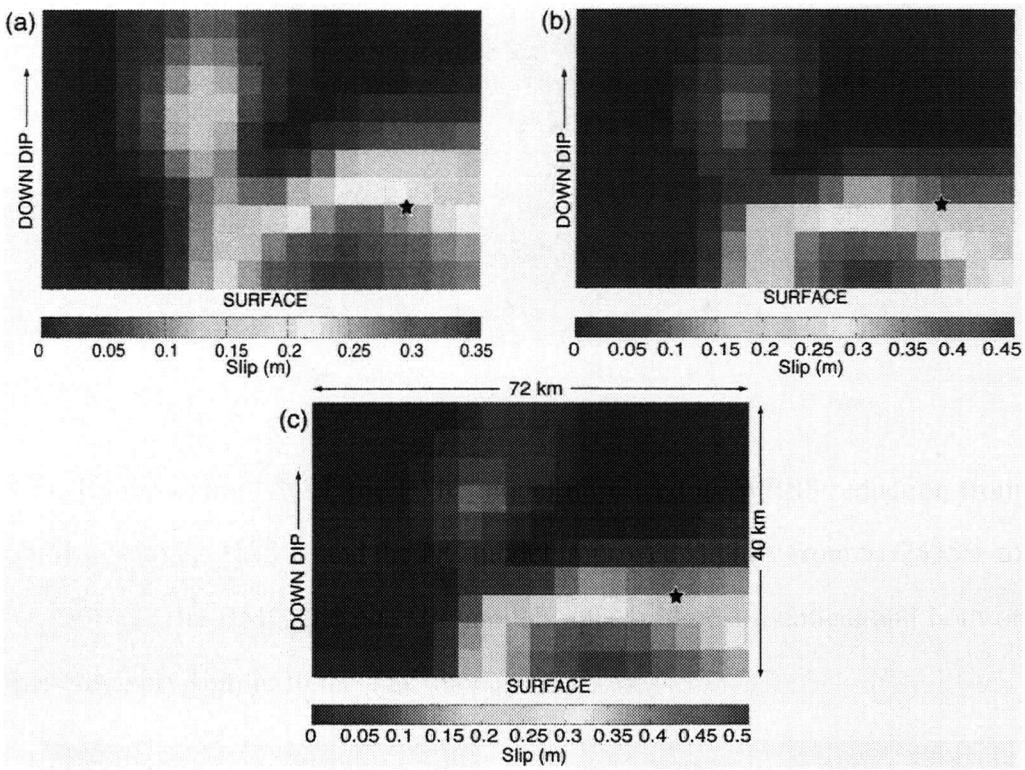

Figure 8.5: 1991-1994 slip inversions using the same GPS sites for all data sets (without site NICH). (a) TSC model (b) BMC model (c) NC model.

Sensitivity to Fault Parameters

As stated in Section 7.1, the fault geometry used for inversion modeling assumed the values of those found by Tan (2005). In order to ascertain how sensitive the

inversion results are to choice of fault geometry, the WRSS reduction found using the TSC data for the 1991-1994 period was compared with WRSS reduction values resulting from using the fault geometries of the other models listed in Table 3.1. A β of 10 km^2/m was used throughout. This was performed in a step-wise process, and Table 8.1 shows how the WRSS reduction was affected by incremental changes in fault parameters to adapt from those of Tan (2005) to either (a) Fuenzalida et al (1997), (b) Triep et al (1995), or (c) the Harvard CMT solution. The published hypocenter depths of these models were not used but rather bracketed, as shown in the last two lines of each sub-table. This was necessary to ensure that the fault plane reached the earth's surface while retaining the 4 km^2 fault tile dimension. The last line of each sub-table (bold-faced) represents the greater diversion from the fault geometry of Tan and is therefore a conservative (over-) estimate of fault geometry difference. As seen in Table 8.1, the effects of the differences in reported fault geometries on WRSS reduction are minor. The actual difference in fault plane location and orientation is relatively small as Figure 8.6 shows.

From Model of Tan to Fuenzalida

Change	WRSS Red. (%)	% Change
(no change)	89.65%	0.0
lat/lon to 42.42°N/43.69°E	89.68%	+0.033%
and strike to 286.7°	89.69%	+0.050%
and dip to 29°, depth to 5.8177 km	89.65%	-0.0046%
and dip to 29°, depth to 3.8785 km	**89.48%**	**-0.19%**

(a)

From Model of Tan to Triep

Change	WRSS Red. (%)	% Change
(no change)	89.65%	0.0
lat/lon to 42.4238°N/43.6643°E	89.60%	-0.053%
and strike to 292.9°	89.46%	-0.21%
and dip to 24°, depth to 4.8808 km	89.59%	-0.069%
and dip to 24°, depth to 3.2539 km	**88.12%**	**-1.70%**

(b)

From Model of Tan to Harvard CMT

Change	WRSS Red. (%)	% Change
(no change)	89.65%	0.0
lat/lon to 42.60°N/43.61°E	3.25%	-96.38%
and strike to 288°	3.08%	-96.56%
and dip to 39°, depth to 22.6555 km	**90.89%**	**+1.38%**

(c)

Table 8.1: Sensitivity of afterslip results to choice of fault plane as measured by changes in WRSS reduction explained by inversion models. Inversions are based on TSC data and a β (smoothing) of 10 km^2/m. Fault geometries begin with the parameters of Tan (2005) and are adapted incrementally to the models of (a) Fuenzalida et al (1997), (b) Triep et al (1995), and (c) Harvard CMT.

The reduction in WRSS obtained using the different fault geometries varies

relatively little. To compare these changes with that of the relatively arbitrary task of choosing a smoothing value (β), the original WRSS reduction of 89.6489% with β = 10 km^2/m changes to 89.8284% with β = 9 km^2/m or 89.4820% with β = 11 km^2/m. These changes correspond to +0.2002% and -0.1862% from 89.6489% respectively.

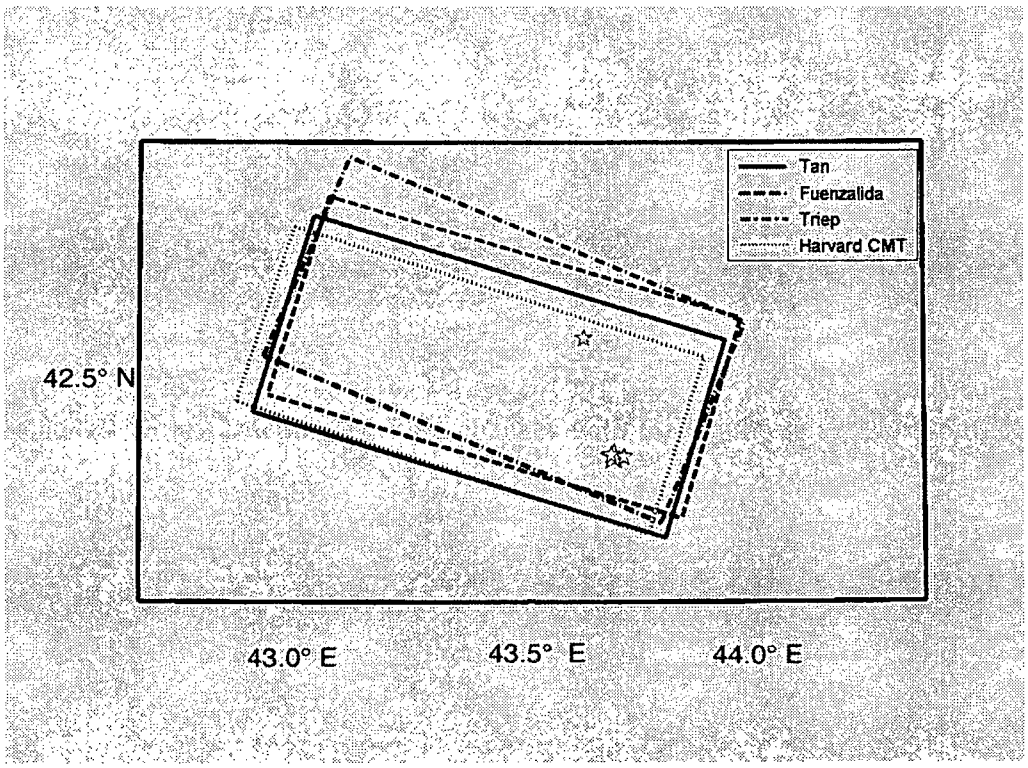

Figure 8.6: Surface outline of the fault plane using the fault geometries of Tan, Fuenzalida, Triep, and Harvard CMT. Stars are the Racha epicenter according to the different groups.

It is not enough to compare just error reduction, rather it is also important to know how much the actual slip solution varies among the different possible fault geometries. This is shown in Figure 8.7 where it can be seen that the slip

distributions resulting from the use of the geometries of Fuenzalida et al (1997) and Triep et al (1995) show the same basic slip pattern as that of Tan (2005). The main difference to be noted is that the modeled slip tends to not extend as far down the plane, especially with the geometry of Triep. The moment of the modeled afterslip is relatively similar as well with 26.0918%, 29.9303%, and 35.451% of the coseismic slip of Tan for the geometries of Fuenzalida, Triep, and Tan respectively.

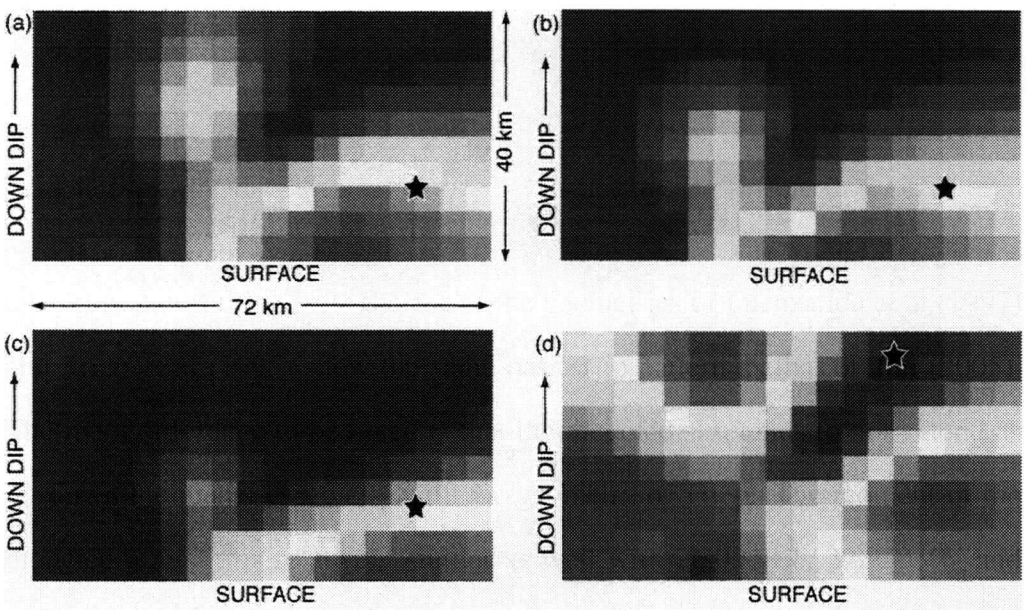

Figure 8.7: Patterns of modeled afterslip using different published fault geometries. Star indicates the Racha hypocenter. (a) Tan (2005), (b) Fuenzalida et al (1997), (c) Triep et al (1995), (d) Harvard CMT.

Determination of Best Smoothing Value β

As indicated in Equation 7.2, smoothing or β acts in the inversion as a weight on how significant the roughness term should be. That is, when minimizing the misfit and roughness, the smoothing determines how important achieving a smoothly varying result should be. As smoothing is increased, results become more evenly distributed and therefore more likely to resemble what happens in nature, though this comes at the cost of not explaining the data as well as a model with less smoothing. There is no obvious way of knowing which smoothing value gives the best trade-off, and choosing one seems to be something of an art.

In all of the inversion results described above, a β of 10 km^2/m was used. This was initially based primarily on trial and error with 10 km^2/m seeming to be on the threshold of β values that produced slip distributions without scattered patches of unrealistic appearing slip. That is, smaller values of β gave slip distributions with faint, disconnected areas of slip that appeared unrealistic in the sense that they were disjointed and erratically distributed. In order to ensure that 10 km^2/m for β was a reasonable choice and to help determine how reliable the patch of deep slip shown in Figure 8.1 may be, two different methods of choosing an optimal smoothing were tested.

The first was simply make a "Tikhonov plot" which is the model's weighted residual sum of squares (WRSS) versus roughness (m^2/km^4) and to find the point on the plot where the curvature between the two is the greatest and then select the corresponding β. This β value is taken as an approximate compromise (e.g. *Hansen*, 1998). The idea is that changing β from this point would cause either of

the following undesirable situations to arise: 1) allowing the misfit to steadily increase while producing only marginal decreases in roughness or 2) allowing the roughness to increase substantially while reaping only minimal improvements in misfit.

The second method tried was the cross validation sum of squares (CVSS) (*Matthews and Segall*, 1993). In this method the optimal β is chosen based on that which allows the most efficient prediction of missing stations. Each station in the GPS network is removed one at a time and inversions are performed with the remaining stations for a variety of β values. The resulting inversions are then forward-modeled for the missing site to find its residuals between the model and data. Once this is done for each site all the squared residuals are summed up according to β value, and it is this sum of residuals that is used to select the optimal β. The β that produces the minimal sum of squared residuals is that considered to be the optimal smoothing value.

The results of these two tests for both types of secular correction (TSC and BMC) are shown in Figure 8.8. The range of optimal β values for the TSC data is 2-4 km^2/m and that for the BMC data is 3-7.5 km^2/m. The differences in amount of WRSS reduction and slip moment between using these β values and 10 km^2/m are shown in Table 8.2. That the deep patch of slip still exists at $\beta = 10$, a higher than "optimal" value which acts to blur the spatial distribution of slip, argues for the believability of this slip.

Comparison of Different Smoothing Values

	β (km^2/m)	WRSS Red.	Moment (N m)	% Coseis. Moment
Data with Time-Series Correction (TSC)	2	91.08%	$6.96 \pm 0.56 \times 10^{18}$	21.78%
	4	90.74%	$7.11 \pm 0.30 \times 10^{18}$	22.26%
	10	89.65%	$7.58 \pm 0.13 \times 10^{18}$	23.74%
Data with Block Model Correction (BMC)	3	66.85%	$5.12 \pm 0.36 \times 10^{18}$	16.04%
	7.5	66.08%	$5.74 \pm 0.16 \times 10^{18}$	17.97%
	10	65.62%	$6.02 \pm 0.13 \times 10^{18}$	18.83%

Table 8.2: Comparison of WRSS reduction and moment resulting from models with different β values. The first two β values for each data set are those determined by the methods of analyzing the trade-off between misfit and roughness and of cross validation sum of squares (CVSS). The third β value, a more conservative 10 km^2/m, is that which was used in many of the tests presented in the results. This value had been chosen due to it allowing for a more reasonable-appearing slip distribution.

Performing the CVSS test also indicated that it is only site KHUR that is responsible for the deep patch of slip shown in Figure 8.1. KHUR happens to lie almost directly above this deeper modeled area of slip, and as seen in Figure 8.2 it is one of the better determined sites in terms of signal to noise (or displacement to error).

To see what the difference in inversion results looks like from using these different β values, Figure 8.9 displays the inversions using the "optimal" β values as well as a β of 10 km^2/m.

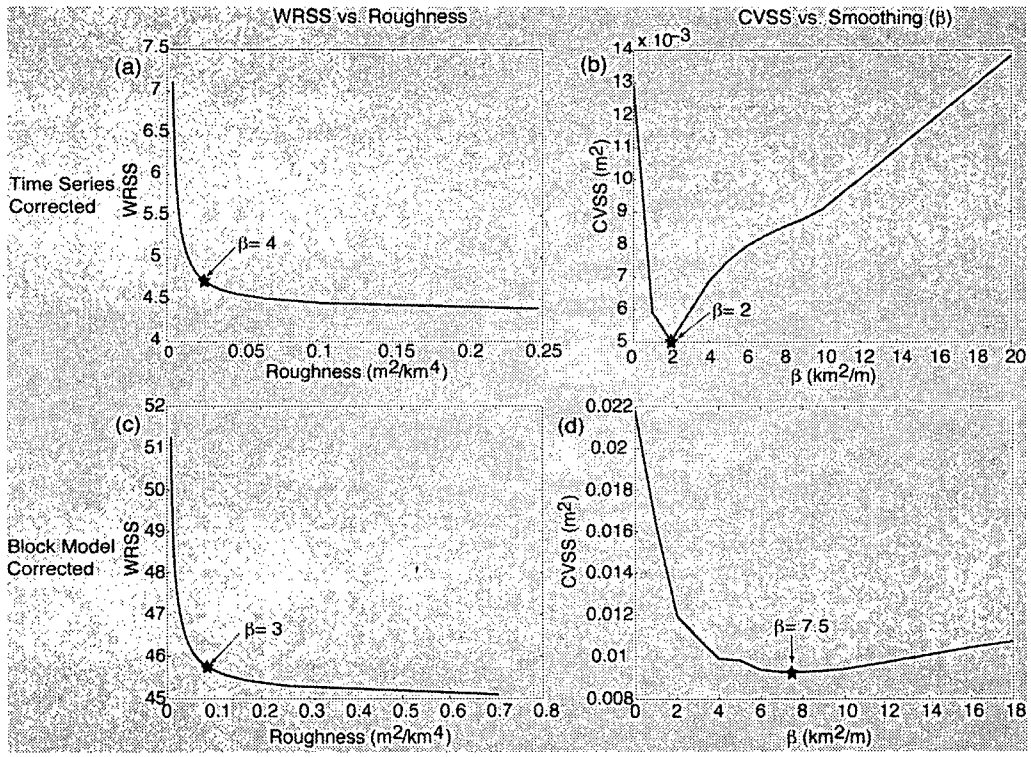

Figure 8.8: Determination of smoothing parameter, β, for TSC data (a,b) and BMC data (c,d). The first method used, a "Tikhonov plot", determines where the change between the weighted residual sum of squares (WRSS) and roughness is greatest (a,c) and then use the associated β. The second method is cross validation sum of squares (CVSS) where β is chosen based on which value produces the smallest sum of residuals. Between the two methods, the optimal value of β ranges from 2 to 4 km^2/m for the TSC data and 3 to 7.5 km^2/m for the BMC data.

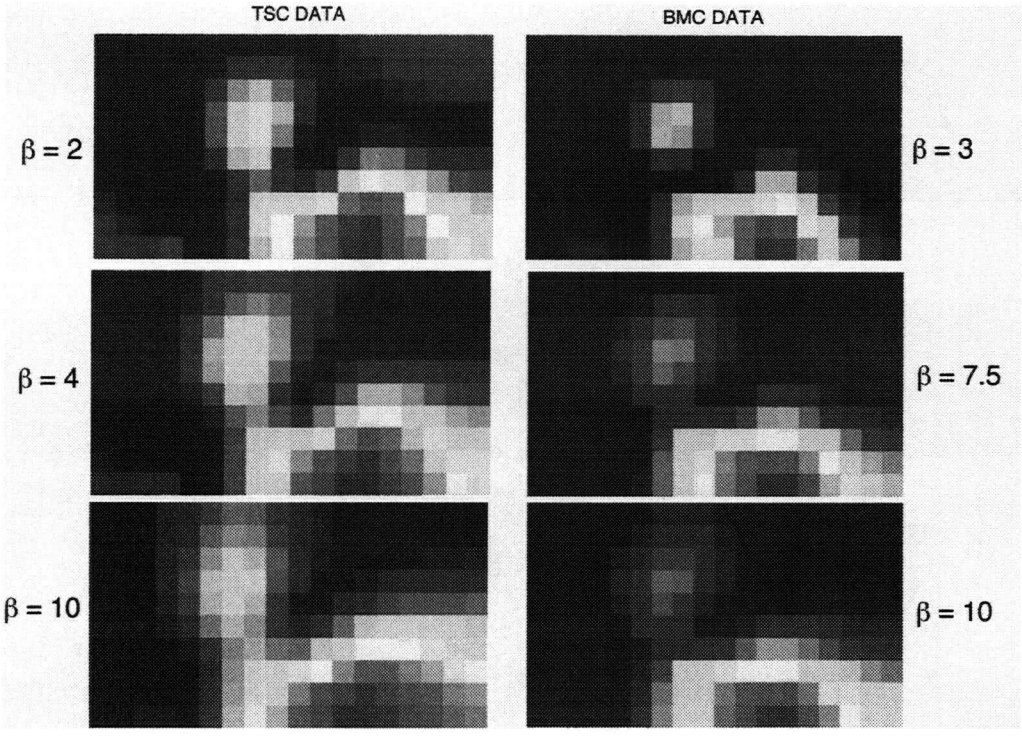

Figure 8.9: Afterslip inversions resulting from use of different smoothing values, β, for TSC and BMC data. The first two smoothing values displayed for each data type are those corresponding to the methods of WRSS versus roughness and of CVSS (see Figure 8.8).

Model Sensitivity to ν

To test of the sensitivity of afterslip inversion results to choice of Poisson's ratio, ν, values 0.03 greater and smaller were used in inversions with TSC and BMC data. Table 8.3 shows these results.

Sensitivity to Poisson's Ratio

Poisson's	TSC Data		BMC Data	
Ratio (ν)	WRSS Red.	Moment (N m)	WRSS Red.	Moment (N m)
0.28	89.707%	7.765×10^{18}	65.905%	6.195×10^{18}
0.25	89.649%	7.585×10^{18}	65.619%	6.015×10^{18}
0.22	89.584%	7.415×10^{18}	65.336%	5.852×10^{18}

Table 8.3: Test for the sensitivity to Poisson's ratio, ν, by increasing and decreasing ν from the value of 0.25 otherwise used. Differences in WRSS reduction and moment are indicated.

Experiment with Slip Constraints

Up to now all afterslip inversions were performed with a dip-slip-only constraint. That is, only dip-slip motion was allowed along the fault as this is consistent with Tan's (2005) coseismic slip model. As there is a small component of right-lateral strike-slip motion along the Greater Caucasus mountains (e.g. *Triep et al*, 1995; *Fuenzalida et al*, 1997), an experiment was tried allowing right-lateral as well as dip-slip motion along the fault. The result is that for the TSC and BMC data the WRSS reduction increased only modestly (89.649% to 90.750% and 65.619% to 67.130% respectively). A similar dip-slip pattern as before resulted, but all of the strike-slip component was placed in a far, deep corner of the fault plane (bottom northwest corner) (see Figure 8.10).

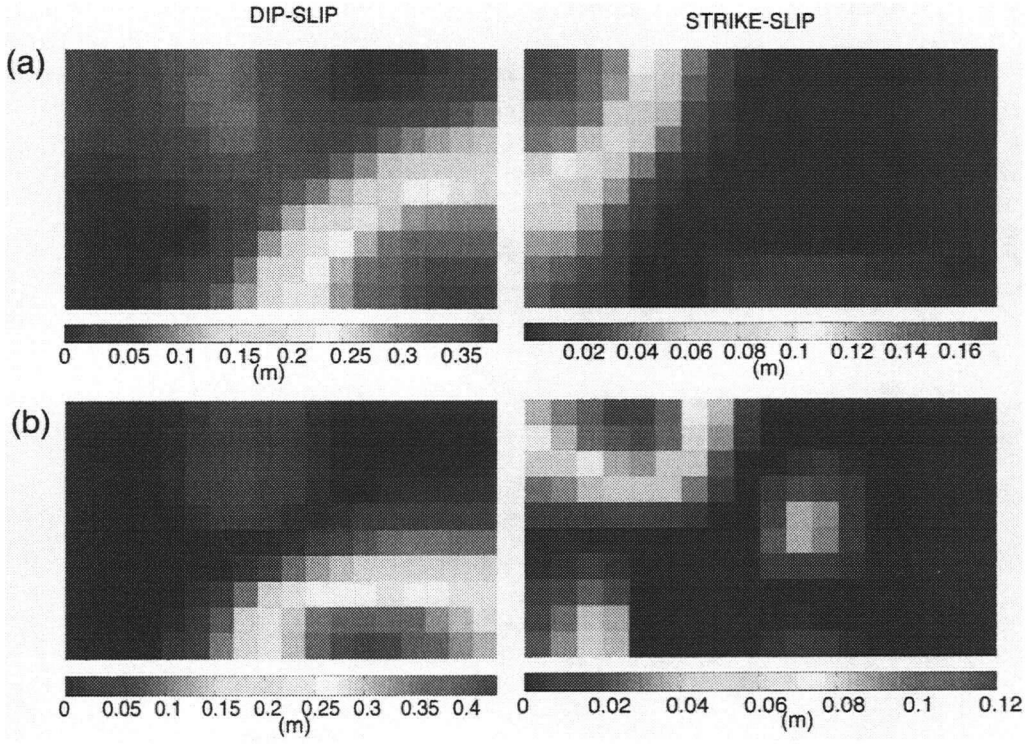

Figure 8.10: 1991-1994 afterslip inversions with dip-slip and strike-slip components using (a) TSC data and (b) BMC data.

1994-1996 Displacements

While it was not expected to be able to detect afterslip much beyond three years following the Racha event (see Other Postseismic Deformation Studies), the 1994-1996 time period was modeled for afterslip to ensure that this was a valid assumption. Figure 8.11 shows these results for the two methods of secular correction. Although similar through the center of the fault plane, these afterslip models do not explain the data very well. Again using a β of 10 km^2/m the WRSS reduction for the TSC and BMC methods were 22.0902% and 24.9727%

respectively. The moments due to each correction type are 2.714×10^{18} N m and 1.247×10^{18} N m respectively. As the 1994-1996 data fit was not good, afterslip was not modeled in later time periods.

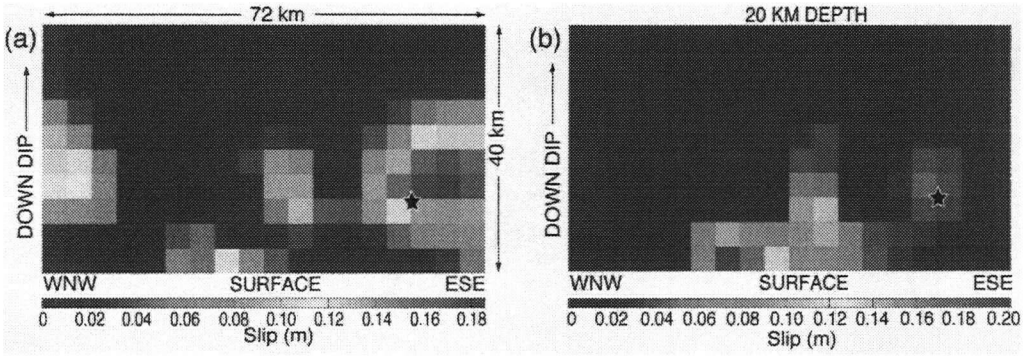

Figure 8.11: 1994-1996 afterslip inversion results (a) using data TSC data and (b) using BMC data. Star on each slip plane represents the Racha hypocenter, and each tile is 4 km square.

8.2 Viscoelastic Relaxation Modeling

1991-1994 Displacements

Viscoelastic Lower Crust

The spherically symmetric viscoelastic forward-modeling code, Visco1D (*Pollitz*, 1992), was used to forward model the Racha mainshock model of Tan (2005). Three different viscoelastic lower crust thicknesses were used: 10 km, 20 km, and 30 km. This thickness is measured upward from the base of the 45 km thick crust. A range of viscosities (1×10^{17} to 1×10^{20} Pa sec) was modeled.

The weighted residual sum of squares (WRSS) was calculated to assess the fit of the viscoelastic models to the data corrected with both the TSC and BMC methods. Contour plots were made of the WRSS against thickness of viscoelastic lower-crust and logarithm of viscosity (Figure 8.12).

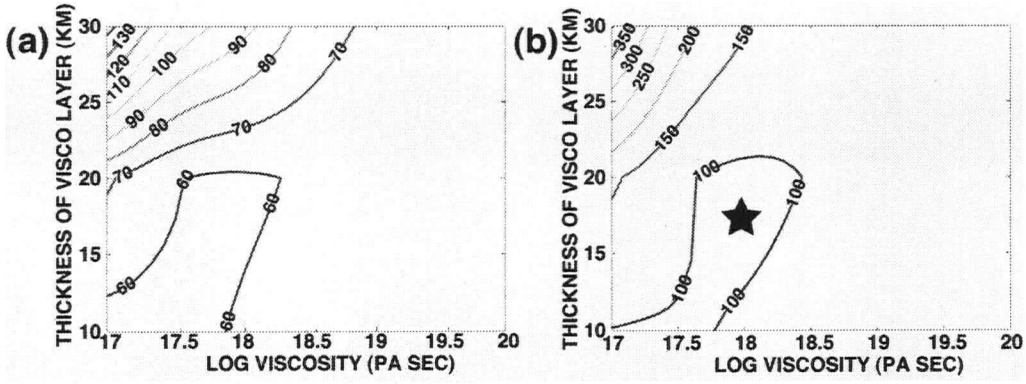

Figure 8.12: Sensitivity of WRSS to lower-crust viscoelastic layer thickness and viscosity. The best model with the TSC data (a) has a viscoelastic lower crust of 10 km thickness and a viscosity of about 1.0×10^{17} Pa sec. The best model (star) with BMC data (b) has a viscoelastic lower-crustal thickness of 10-18 km and a viscosity of about $2.5 - 6 \times 10^{17}$ Pa sec.

The viscoelastic lower-crust models show the best fit to the TSC data with a layer thickness of 10 km and a viscosity of about 1×10^{17} Pa sec with a WRSS reduction of about 19%. The viscoelastic lower-crust models have a minimum WRSS for the BMC data with a layer thickness of about 15-20 km and a viscosity of 5×10^{17} to 1×10^{18} Pa sec (Figure 8.12b). This corresponds to a WRSS reduction of about 21%. Neither set of GPS data is well modeled as viscoelastic relaxation of a lower-crustal layer.

The vectors of these best models are compared against data in Figure 8.13.

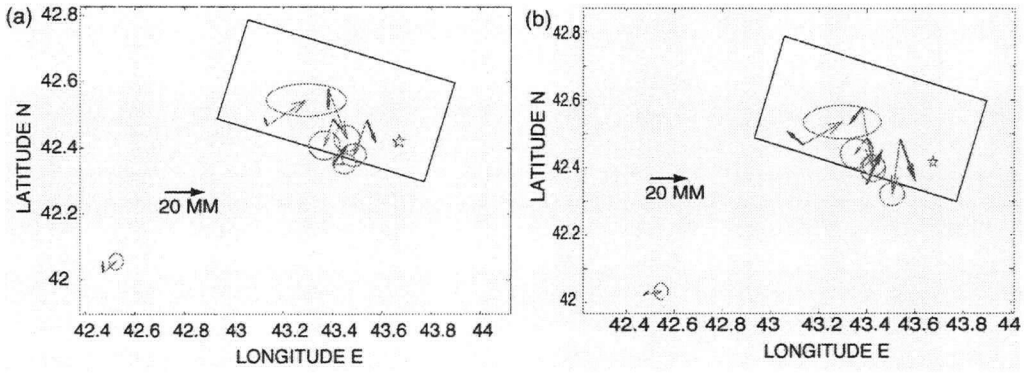

Figure 8.13: Displacement vectors from best fitting Visco1D models and 1991-1994 GPS site displacements. (a) TSC data with a viscoelastic lower crust at 35-45 km with a viscosity of 1 $\times 10^{17}$ Pa sec. (b) BMC data with a viscoelastic lower crust at 25-45 km with a viscosity of 9 $\times 10^{17}$ Pa sec. Star is the Racha epicenter.

Viscoelastic Mantle Half-Space

The results of modeling a viscoelastic mantle half-space are indicated in Figure 8.14. The best fitting model for both TSC and BMC data sets has a viscosity of about 2 $\times 10^{18}$ Pa sec corresponding to a WRSS reduction of about 5-8%.

1996-2000 Displacements

As stated previously, the TSC data don't allow the possibility of testing for post-seismic deformation during the 1996-2000 time period. The block model corrected (BMC) data, however, are not subject to this restriction.

Lower-crustal viscoelastic relaxation was modeled for an array of viscosity values. A layer thickness of 20 km (25-45 km depth) was used as this is the thickness that best fit the data for the 1991-1994 period. The best fitting 1991-

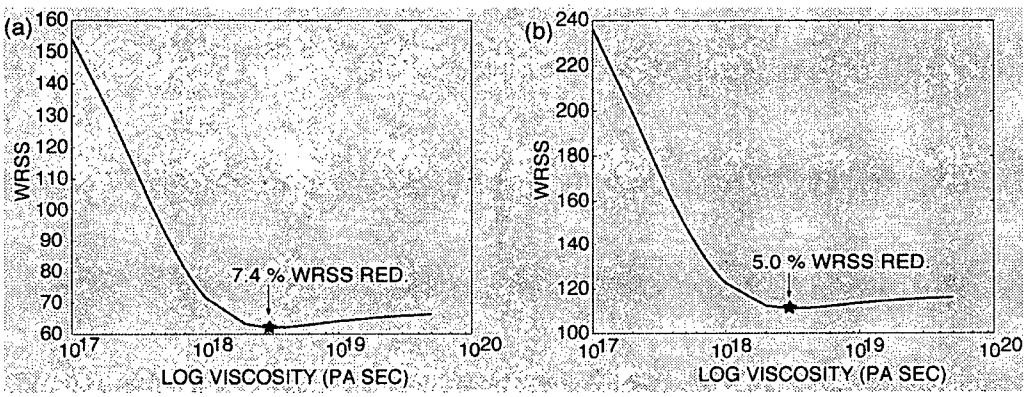

Figure 8.14: WRSS versus logarithm of viscosity for forward-modeled viscoelastic mantle half-space models compared with (a) TSC data and (b) BMC data.

1994 BMC model has a viscosity of 9×10^{17} Pa sec (and a 20 km thickness). The WRSS reduction with this viscosity and thickness for the 1996-2000 data is less than 0%, a very poor fit. Figure 8.15 shows that the best fit to the 1996-2000 data produces about a 25% WRSS reduction with a viscosity of about 10^{19} Pa sec.

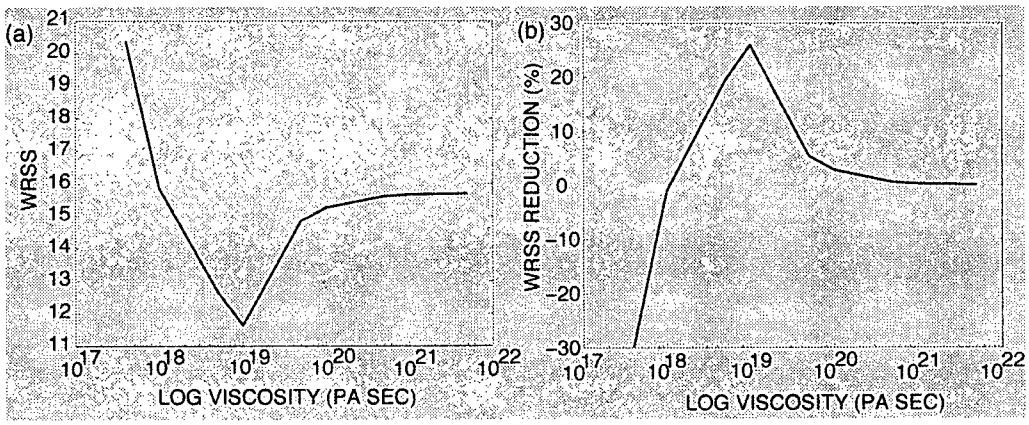

Figure 8.15: Comparison between BMC data and models of a 20 km thick viscoelastic lower crust (25-45 km depth). (a) WRSS versus logarithm of viscosity. (b) Corresponding WRSS reduction versus logarithm of viscosity.

Chapter 9

Discussion

9.1 Secular Correction of GPS Data

Since no GPS sites were established in the region surrounding the Racha earthquake prior to its occurrence, pre-earthquake site velocities were unavailable. This spawned the search for other correction methods, and two were used throughout this study. The first method is the time-series correction (TSC) that assumes that all or most postseismic deformation was over within the first five years and which used the 1996-2000 period of the GPS data set to estimate the secular deformation rate. The second method is the block model correction (BMC) that used the results of a tectonic block model to estimate the secular deformation.

Both correction methods have their limitations. The TSC method may indeed introduce an overcompensation in that there could still be a postseismic signal contained in the 1996-2000 time-series that gets subtracted from the first period

of the time-series. The BMC method is based on a model that is spatially coarse relative to the physical dimensions of this study. It also contains only horizontal motions, so that the vertical component does not get corrected for secular displacement by this method. Finally, the BMC method is based on a model that includes the entire seismic cycle and not just the preseismic period. This is a problem because deformation rates and patterns around a fault can change between earthquakes (*Savage and Prescott*, 1978). Due to these uncertainties in the two correction methods, both were employed throughout with the outcome that similar results were obtained. That both methods obtain similar results lends confidence to these findings that would not be achieved by either method alone.

To otherwise compare how significant the choice of secular correction method is, the data were modeled for afterslip with no correction for secular deformation. Although the WRSS is much less impressive (52% versus 66% or 90%), the overall pattern of afterslip is still very similar (Figure 8.5). This shows that no matter how the data are secularly corrected, there is little effect on the inferred pattern of afterslip. That the secularly corrected data are much better fit by the model indicates that the secular correction methods employed are valid, perhaps one (TSC) more so than the other (BMC).

Figure 8.4 shows why the TSC correction method results in such a better WRSS reduction. While the near-field GPS sites are fit reasonably well by the two secular correction methods and by no correction, it is the far-field sites that are fit best by the TSC method. This shows again that the TSC data is probably the most appropriate or accurate to use and by extension that the assumption of

no postseismic deformation after five years is likely reasonable.

9.2 Afterslip and Viscoelastic Relaxation Models

1991-1994 Displacements

The 1991-1994 data set was best fit by an afterslip model that explained about 90% of the data. By comparison, the best viscoelastic model produced a WRSS reduction of only 21%. To see what this difference in model fit looks like in term of displacement vectors, a comparison of Figures 8.2a and 8.13b shows that the afterslip model closely mimics the data while the viscoelastic model bears very little actual resemblance.

Due to differences in the modeled afterslip moment from using different values of smoothing parameter (β) and due to uncertainties in choosing an appropriate value for β, the moments produced by the TSC data are about 22-24% of the coseismic moment (with a β range of 2-10 km^2/m). (β=2 km^2/m results from the CVSS method, and the conservative value of β=10 km^2/m is used throughout most of the modeling and testing.) This afterslip moment release is on the high end though still similar to other studies that found afterslip in the immediate postseismic period with values of 10-22% of the coseismic moment being reported (e.g. *Yu et al*, 2003; *Donnellan and Lyzenga*,1998; *Segall et al*, 2000).

This must still be approached with some caution, however, as the start of the GPS time-series was about 2.75 months after the Racha event, and a sizable amount of afterslip may have occurred undetected during this time. For example,

in the first three months after the Chi-Chi earthquake about 7% of the coseismic moment was detected in afterslip (*Hsu et al*, 2002). So, the actual postseismic moment release following the Racha earthquake may be something larger than 22% of the coseismic moment. On the other hand, the afterslip predicted by the elastic half-space model may be an overestimate due to a rock type contrast across the fault zone. The crystalline basement Dzirula Massif that comprises the footwall may be expected to deform less than the sedimentary Gagra-Dzhava zone that makes up the hanging wall due to the rocks of the hanging wall being less dense and weaker than those of the footwall. As most of the GPS stations sit on the hanging wall the inversion is mainly trying to fit these hanging wall displacements. As the model contains no difference in rock type across the fault, the slip inversion may be prescribing too much slip as it is almost exclusively fitting displacements of the weaker hanging wall. (If there were more stations on the footwall, the inversion would be more balanced.)

Considering the possibilities in choosing fault parameters based on published studies of the source geometry, the differences in data explanation with all other factors equal are generally smaller than those of the aforementioned β range. For example, the range of WRSS reduction from using any of the three available fault geometries based on teleseismic body waves (at β=10 km^2/m) is 88.123-89.649% while that from the a β range of 2-10 km^2/m (with the Tan fault geometry) is 89.649-91.079%.

When allowing strike-slip as well as dip-slip afterslip motion, the meager improvement in WRSS reduction does not justify the inclusion of the strike-

slip component. Also, according to the kinematic model this strike-slip motion would have to occur in a completely different area of the fault plane which is the very corner (northwest) where the GPS network is not able to resolve slip (Figure 7.3).

Adjusting Poisson's ratio up or down by 0.03 from 0.25 did not produce a significant effect in data explanation or afterslip moment. Therefore the choice of the typically used value of 0.25 seems to be reasonable.

As expected given the relatively small size of the earthquake and local scale of deformation, viscoelastic relaxation of the mantle is not responsible for observed early postseismic deformation as has been suggested for other earthquakes (e.g., *Pollitz*, 2000).

Comparison of Afterslip with Aftershocks

A comparison of afterslip with the distribution of aftershocks (*Fuenzalida et al*, 1997) shows that the two generally do not overlap (Figure 9.1). While these aftershock data were collected in the two months between the Racha event and the first GPS position measurement, they provide a good overall picture of the distribution of aftershocks. One can also assume that afterslip that occurred before the first GPS measurement was in a similar location. It is noteworthy that the deep patch of the afterslip happens to fall in an area with no aftershocks but which is bounded on three sides by significant aftershock activity. This seems to indicate that this section of the fault deforms aseismically and that it loads the surrounding region.

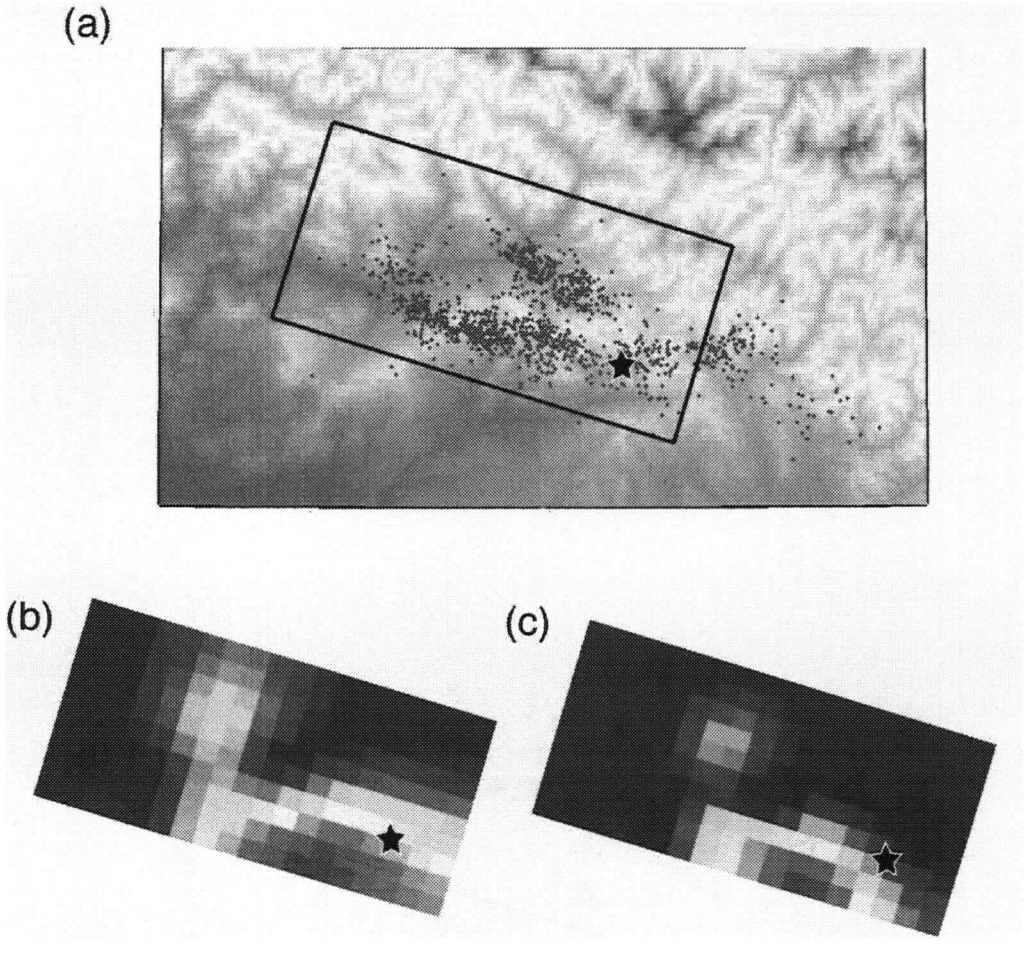

Figure 9.1: (a) Aftershocks over the two months following the Racha event (May 10, 1991 to July 9, 1991) (*Fuenzalida et al*, 1997). Afterslip fault plane is outlined. Star represents Racha hypocenter and can be used with fault plane outline to compare aftershocks with 1991-1994 (b) TSC afterslip and (c) BMC afterslip. The afterslip models are from data covering the period July 25, 1991 to October 10, 1994.

The 1991-1994 afterslip moment was compared with seismic moment from aftershocks during the same time period over the area of the afterslip fault plane. The aftershocks used were from the Incorporated Research Institutions for Seismology (IRIS) which provide a compilation of events from different earthquake catalogs. The total moment of these events summed to 2.4461×10^{16} N m. This is far less than the moment release from afterslip (7.112×10^{18} N m) which shows that aseismic deformation is required by the GPS data. This difference in moment between afterslip and aftershocks is comparable to that found in Loma Prieta, California (*Bürgmann et al*, 1997).

Post-1994 Displacements

To test if afterslip continued beyond 1994, the 1994-1996 time period was modeled for afterslip with the result that no pattern of afterslip could accurately explain either the TSC or BMC data.

As viscoelastic relaxation can manifest itself later in the postseismic period, the 1996-2000 BMC data were modeled with the result that the best viscoelastic model could explain only 25% of the data. Very low viscosities ($< 10^{18}$ Pa sec) produce models with negative WRSS reduction. That is, at these low viscosities modeling produces displacement vectors that are much larger than the data. According to these results, lower-crust viscosities less than 10^{18} Pa sec can be ruled out. This can place constraints on theoretical models of continental collision models. For example Pysklywec et al (2002) model a continental collision zone using a lower-crustal rheology of wet quartz which has a viscosity on the

order of 10^{17} Pa sec. If the results presented here hold for other continental collision zones in general, such a low viscosity can be dismissed as unreasonable. Moderately low viscosities ($> 10^{19}$ Pa sec) cannot necessarily be dismissed because models with such viscosity values yield too little surface deformation to be resolved with campaign-model GPS.

Chapter 10

Conclusions

It was found that postseismic deformation after the Racha earthquake was due to afterslip. Most afterslip was shallow, though a patch at 10-16 km depth was identified. Slip could be resolved only west of the hypocenter. Though the TSC data, Tan's fault geometry, only dip-slip on the coseismic rupture plane, and a β of 4 km^2/m are preferred, these findings hold even when these constraints are relaxed. The final WRSS reduction and afterslip moment over the 1991-1994 time period given the above parameter choices is 91% and $7.112 \pm 0.295 \times 10^{18}$ N m respectively. (The uncertainty in moment results from the uncertainty in slip produced by the inversion code.) This moment corresponds to 22.2± 0.9% of the coseismic slip of Tan (2005), and only 0.34% of this afterslip can be attributed to aftershocks.

Viscoelastic models did not fit the GPS data well and afterslip was found to be the dominant mechanism of postseismic deformation in the first three years

following the Racha earthquake. However, the existence of a viscoelastic lower crust or upper mantle in the western Greater Caucasus cannot be ruled out as it may simply be that this event was not large enough to excite a noticeable viscoelastic response.

Bibliography

Alexidze, M.A., Gugunava, G.E., Kiria, D.K., and Chelidze, T.L., A three-dimensional stationary model of the thermal and thermoelastic fields of the Caucasus, *Tectonophysics, 227*, 191-203, 1993.

Al-Lazki, A.I., Seber, D., Sandvol, E., Turkelli, N., Mohamad, R., and Barazangi, M., Tomographic Pn velocity and anisotropy structure beneath the Anatolian plateau (eastern Turkey) and the surrounding regions, *Geophys. Res. Lett., 30*, 8043-8047, 2003.

Altamimi, Z., P. Sillard, and C. Boucher, ITRF2000: A new release of the International Terrestrial Reference Frame for earth science applications, *J. Geophys. Res, 107*, 2214-2233, 2002.

Asanidze, B.Z., Pecherksy, D.M., and Adamia, Sh.A., Results of paleomagnetic studies of Paleozoic rocks in the Caucasus (in Russian), Izv. Acad. Sci. USSR, *Phys. Solid Earth*, Engl. Transl., 34-48, 1980.

Balavadze, B.K., Shengelaya, G.Sh., and Mindel, P.Sh., A gravitational model of the earth crust for the Caucasus and Caspian Sea area, In: Gravitational Models of the Earth Crust and Upper Mantle, emphNarkova Dumka, Kiev.

Blanpied, M.L., D.A. Lockner, and J.D. Byerlee, Fault stability inferred from granite sliding experiments at hydrothermal conditions, *Geophys. Res. Lett., 18*, 609-612, 1991.

Bürgmann, R., S. Ergintav, P. Segall, E. Hearn, S. McClusky, R. Reilinger, H. Woith, and J. Zschau, Time-dependent distributed afterslip on and deep below the İzmit earthquake rupture, *Bull. Seism. Soc. Am., 92* 126-137, 2002.

Bürgmann, R., Segall, P., Lisowski, M., and Svarc, J., Postseismic strain following the 1989 Loma Prieta earthquake from GPS and leveling measurements, *J. Geophys. Res., 102*, 4933-4955, 1997.

Burtman, V.S., Kinematics of the Arabian syntaxis, *Geotectonics, 23*, 139-146, 1989.

Chang, C.H., Y.M. Wu, T.C. Shin, and C.Y. Wang, Relocation of the 1999 Chi-Chi earthquake in Taiwan, *Terr. Atmos. Oceanic Sci., 11*, 581-590, 2000.

Cohen, S.C., A multilayer model of time dependent deformation following an earthquake on a strike slip fault, *J. Geophys. Res., 87*, 5409-5421, 1982.

DeMets, C., R.G. Gordon, D.F. Argus, and S. Stein, Current plate motions, *Geophys. J. Int., 101*, 425-478, 1990.

DeMets, C., Gordon, R.G., Argus, D.F., and Stein, S., Effects of recent revisions to the geomagnetic reversal time scale on estimates of current plate motions, *Geophys. Res. Lett., 21*, 2191-2194, 1994.

Deng, J.M., H. Kanamori, and E. Hauksson, Viscoelastic flow in the upper crust after the 1992 Landers, California earthquake, *Science, 282*, 1689-

1692, 1998.

Dietrich, J.H., Modeling of rock friction: 1. experimental results and constitutive equations, *J. Geophys. Res., 84*, 2161-2168, 1979.ling of rock friction: 1. experimental results and constitutive equations, *J. Geophys. Res., 84*, 2161-2168, 1979.

Dietz, L.D. and Ellsworth, W.L., The October 17, 1989, Loma Prieta, California, earthquake and its aftershocks: Geometry of the sequence from high-resolution locations, *Geophys. Res. Lett., 17*, 1417-1420, 1990.

Dixon, T.H., An introduction to the global positioning system and some geological applications, *Rev. of Geophys, 29*, 249-276, 1991.

Donnellan, A. and G.A. Lyzenga, GPS observations of fault afterslip and upper crustal deformation following the Northridge earthquake, *J. Geophys. Res., 103*, 21285-21297, 1998.

Dotduyev, S.I., Nappe structure of the Greater Caucasus Range, *Geotectonics, 20*, 420-430, 1986.

Dziewonski, A.M. and Anderson, D.L., Preliminary reference Earth model, *Phys. Earth Plan. Interiors, 25*, 297-356, 1981.

Elasser, W.M., Convection and stress propagation in the upper mantle, in The Application of Modern Physics to the Earth and Planetary Interiors, *Wiley-Interscience*, 1969.

Fialko, Y. Evidence of fluid-filled upper crust from observations of postseismic deformation due to the 1992 M_w 7.3 Landers earthquake,

J. Geophys. Res., 109, B08401, doi:10.1029/2004JB002985, 2004.

Freed, A.M. and R. Bürgmann, Evidence of power-law flow in the Mojave desert mantle, *Nature, 430*, 548-551, 2004.

Freed, A.M., R. Bürgmann, E. Calais, J. Freymueller, and S. Hreinsdóttir, Implications of deformation following the 2002 Denali, Alaska, earthquake for postseismic relaxation processes and lithospheric rheology, *J. Geophys. Res., 111*, B01401, doi:10.1029/2005JB003894, 2006.

Fuenzalida, H., Rivera, L., Haessler, H., Legrand, D., Philip, H., Dorbath, L., McCormack, D., Arefiev, S., Langer, C., and Cisternas, A., Seismic source study of the Racha-Dzhava (Georgia) earthquake from aftershocks and broad-band teleseismic body-wave records: an example of active nappe tectonics, *Geophys. J. Int., 130*, 29-46, 1997.

Fung, Y.C., Foundations of Solid Mechanics, (Prentice-Hall, Englewood Cliffs, NJ, p. 425, 1965)

Hansen, P.C., Rank-Deficient and Discrete Ill-Posed Problems, *Society for Industrial and Applied Mathematics*, 1998.

Hearn, E.H., B.H. Hager, R.E. Reilinger, Viscoelastic deformation from North Anatolian Fault Zone earthquakes and the eastern Mediterranean GPS velocity field, *Geophys. Res. Lett., 29*, 10.1029/2002GL014889, 2002.

Hetland, E.A. and B.H. Hager, Postseismic and interseismic displacements near a strike-slip fault: A two-dimensional theory for general linear viscoelastic rheologies, *J. Geophys. Res., 110*, B10401,

doi:10.1029/2005JB003689, 2005.

Hreinsdottir, S., Freymueller, J.T., Fletcher, H.J., Larsen, C.F., and Burgmann, R., Coseismic slip distribution of the 2002 Mw7.9 Denali fault earthquake, Alaska, determined from GPS measurements, *Geophys. Res. Lett., 30*, 1670-1674.

Hsu, Y.J., N. Bechor, P. Segall, S.B. Yu, L.C. Kao, and K.F. Ma, Rapid afterslip following the 1999 Chi-Chi, Taiwan earthquake, *Geophys. Res. Lett., 29*(16), 1974, doi:10.1029/2002GL014967, 2002.

Jackson, I., Peterson, M.S., and FitzGerald, J.D., Seismic wave dispersion and attenuation in Aheim dunite: an experimental study, *Geophys. J. Int., 108*, 517-534, 1992.

Jackson, J., Partitioning of strike-slip and convergent motion between Eurasia and Arabia in eastern Turkey and the Caucasus, *J. Geophys. Res., 97*, 12471-12479, 1992.

Johnson, K.M., Segall, P., and Yu, S.B., A viscoelastic earthquake cycle model for Taiwan, *J. Geophys. Res., 110*, 1029/2004JB003516, 2005.

Kampfmann, W. and Berckhemer, H., High temperature experiments on the elastic and anelastic behavior of magmatic rocks, *Phys. Earth Planet. Inter., 40*, 223-247, 1985.

King, R.W. and Y. Bock, Documentation of the MIT GPS analysis software: GAMIT, Mass. Inst. of Technol., Cambridge, 2004.

Kopp, M.L. and I.G. Shcherba, History of late Alpine development of the

eastern Caucasus, *Geotechnika, 6*, 94-108, 1985.

Marone, C.J., Scholz, C.H., Bilham, R., On the mechanics of earthquake afterslip, *J. Geophys. Res., 96*, 8441-8452, 1991.

Matthews, M. and P. Segall, Statistical inversion of crustal deformation data and estimation of the depth distribution of slip in the 1906 earthquake, *J. Geophys. Res., 98*, 12153-12163, 1993.

McKenzie, D.P., Plate tectonics of the Mediterranean Region, *Nature, 226*, 239-243, 1970.

McKenzie, D.P., Active tectonics of the Mediterranean region, *Geophys. J. R. Astron. Soc., 30*, 109-185, 1972.

McClusky, S., *Personal Communication*, 2006.

Okada, Y., Surface deformation due to shear and tensile faults in a half-space, *Bull. Seis. Soc. Amer., 75*, 1135-1154, 1985.

Owen, S., G. Anderson, D.C. Agnew, H. Johnson, K. Hurst, R. Reilinger, Z.-K. Shen, J. Svarc, and T. Baker, Early postseismic deformation from the 16 October 1999 M_w 7.1 Hector Mine, California earthquake as measured by survey-mode GPS, *Bull. Seis. Soc. Amer., 92*, 1423-1432, 2002.

Peltzer G., P. Rosen, and F. Rogez, Poroelastic rebound along the Landers 1992 earthquake surface rupture, *J. Geophys. Res., 103*, 30131-30145, 1998.

Peltzer G., P. Rosen, F. Rogez, and K. Hudnut, Postseismic rebound in fault step-overs caused by pore fluid flow, *Science, 273*, 1202-1204, 1996.

Philip, H., Cisternas, A., Gvishani, A., and Gorshkov, A., The Caucasus: an actual example of the initial stages of continental collision, *Tectonophysics,*

161, 1-21, 1989.

Pollitz, F.F., Gravitational viscoelastic postseismic relaxation on a layered spherical Earth, *J. Geophys. Res., 102*, 17921-17941, 1997.

Pollitz, F.F., Postseismic relaxation theory on the spherical Earth, *Bull. Seismol. Soc. Am., 82*, 422-453, 1992.

Pollitz, F.F., G. Peltzer, R. Bürgmann, Mobility of continental mantle: Evidence from postseismic geodetic observations following the 1992 Landers earthquake, *J. Geophys. Res., 105*, 8035-8054, 2000.

Pysklywec, R.N., C. Beaumont, and P. Fullsack, Lithospheric deformation during the early stages of continental collision: Numerical experiments and comparison with South Island, New Zealand, *J. Geophys. Res., 107*, 10.1029/2001JB000252, 2002.

Reilinger, R., S. Erigintav, R. Bürgmann, S. McClusky, O. Lenk, A. Barka, O. Gurkan, E. Hearn, K.L. Feigl, R. Cakmak, B. Aktug, H. Ozener, and M.N. Toksöz, Coseismic and postseismic fault slip for the 17 August 1999, M = 7.5, İzmit, Turkey earthquake, *Science, 289*, 1519-1524, 2000.

Reilinger, R., McClusky, S.C., Oral, M.B., King, R.W., Toksoez, M.N., Barka, A.A., Kinik, I., Lenk, O., and Sanli, I., Global Positioning System measurements of present-day crustal movements in the Arabia-Africa-Eurasia plate collision zone, *J. Geophys. Res., 102*, 9983-9999, 1997.

Reilinger, R., McClusky, S., Vernant, P., Lawrence, S., Ergintav, S., Cakmak, R., Kadirov, F., Guliev, I., Stepanyan, R., Nadariya, M., Hahubia, G., Mahmoud, S., Sakr, K., ArRajehi, A., Paradissis, D., Al-Aydrus, A.,

Prilepin, M., Guseva, T., Evren, E., Dmitrotsa, A., Filikov, S.V., Gomez, F., Al-Ghazzi, R., and Karam, G., GPS constraints on continental deformation in the Africa-Arabia, Eurasia continental collision zone and implications for the dynamics of plate interactions, *in press*, 2006.

Ruina, A.L., Slip instability and state variable friction laws, *J. Geophys. Res., 88*, 10359-10370, 1983.

Ruppel, C. and McNutt, M., Regional compensation of the Greater Caucasus mountains based on an analysis of Bouguer gravity data, *Earth Planet. Sci. Letters, 98*, 360-379, 1990.

Sarker, G. and Abers, G.A., Deep structures along the boundary of a collisional belt: attenuation tomography of P and S waves in the Greater Caucasus, *Geophys. J. Int., 133*, 326-340, 1998.

Savage, J.C. and Burford, R.O., Geodetic determination of relative plate motion in central California, *J. Geophys. Res., 78*, 832-845, 1973.

Savage, J.C and W.H. Prescott, Asthenosphere readjustment and the earthquake cycle, *J. Geophys. Res., 83*, 3369-3376, 1978.

Savage, J.C. and J.L. Svarc, Postseismic deformation associated with the 1992 M_w = 7.3 Landers earthquake, southern California, *J. Geophys. Res., 102*, 7565-7577, 1997.

Segall, P., Burgmann, R., and Matthews, M., Time-dependent triggered afterslip following the 1989 Loma Prieta earthquake, *J. Geophys. Res., 105*, 5615-5634, 2000.

Sheu, S.Y. and Shieh, C.F., Viscoelastic-afterslip concurrence: a possible

mechanism in the early post-seismic deformation of the Mw 7.6, 1999 Chi-Chi (Taiwan) earthquake, *Geophys. J. Int., 159*, 1112-1124, 2004.

Smith, D.E., Kolenkiewics, R., Robbins, J.W., Dunn, P.J., and Torrence, M.H., Horizontal crustal motion in the central and eastern Mediterranean inferred from Satellite Laser Ranging measurement, *Geophys. Res. Lett., 21*, 1979-1982. 1994.

Stark, P.B. and R.L. Parker, Bounded-variable least-squares: An algorithm and application, *Comput. Stat., 10*, 129-141, 1995.

Steketee, J.A., On Volterra's dislocation in a semi-infinite elastic medium, *Can. J. Phys., 36*, 192-205, 1958.

Tan, O., personal communication, 2005.

Triep, E.G., G.A. Abers, A.L. Lerner-Lam, V. Mishatkin, N. Zakharchenko, and O. Starovoit, Active thrust front of the Greater Caucasus: The April 29, 1991 Racha earthquake sequence and its tectonic implications, *J. Geophys. Res., 100*, 4011-4033, 1995.

Tse, S.T. and J.R. Rice, Crustal earthquake instability in relation to the depth variation of frictional slip properties, *J. Geophys. Res., 91*, 9452-9472, 1986.

Turcotte, D.L. and G. Schubert, Geodynamics, *Cambridge University Press*, 2002.

Yu, S.B., Hsu, Y.J., Kuo, L.C., and Chen, H.Y., GPS measurement of postseismic deformation following the 1999 Chi-Chi, Taiwan, earthquake, *J. Geophys. Res., 108*, 2520-2535, 2003.

Yu, T.-T., J.B. Rundle, and J. Fernandez, Surface deformation due to a strike-

slip fault in an elastic gravitational layer overlying a viscoelastic gravitational half-space, *J. Geophys. Res., 101*, 3199-3214, 1996.

Zonenshain, L.P., M.I. Kuzmin, and L.M. Natapov, Alpine-Himalayan Fold-belt within the USSR, in Geology of the USSR, A Plate-Tectonic Synthesis, Geodyn. Ser., vol. 21, edited by B.M. Page, pp. 167-179, *AGU*, Washington, D.C., 1990.

Appendix A

GPS Position Measurements

GPS measurements in ITRF2000 reference frame: top number is the measurement (m) and the second number the 1-σ error. 'ND' means that no data were no available for these stations/times.

GPS POSITION DATA IN ITRF2000

SITE	DIR	1991.563	1994.766	1996.739	1998.711	2000.758
KHOT	N	4.84527	4.89303	4.92217	4.93942	4.96993
	±	0.00575	0.00206	0.00191	0.00169	0.00298
	E	1.84394	1.94697	2.00204	2.06145	2.10662
	±	0.02016	0.00199	0.00182	0.00198	0.00520
	U	1.86131	1.92139	1.90792	1.91190	1.93312
	±	0.03317	0.01131	0.00933	0.00901	0.01610
KHUR	N	2.36334	2.37622	2.39601	2.41212	2.43549
	±	0.00451	0.00193	0.00109	0.00145	0.00283
	E	7.61391	7.70199	7.75830	7.80795	7.85687
	±	0.00626	0.00190	0.00112	0.00171	0.00522
	U	2.39668	2.46641	2.45516	2.45531	2.47293
	±	0.02813	0.01087	0.00532	0.00817	0.01499

SITE	DIR	1991.563	1994.766	1996.739	1998.711	2000.758
LESO	N	7.85791	7.87400	7.89575	7.91382	ND
	±	0.00390	0.00164	0.00116	0.00131	ND
	E	0.81795	0.89633	0.95746	1.00992	ND
	±	0.00621	0.00160	0.00149	0.00140	ND
	U	0.65077	0.74676	0.73975	0.74823	ND
	±	0.02743	0.00805	0.00550	0.00681	ND
NICH	N	7.52641	7.57876	7.60789	ND	ND
	±	0.00308	0.00084	0.00121	ND	ND
	E	1.27515	1.35474	1.41534	ND	ND
	±	0.00347	0.00109	0.00161	ND	ND
	U	9.79525	9.88275	9.87612	ND	ND
	±	0.02637	0.00376	0.00614	ND	ND
SACC	N	1.61635	1.66415	1.69377	ND	1.75325
	±	0.00277	0.00254	0.00130	ND	0.00284
	E	8.96247	9.04982	9.11276	ND	9.21484
	±	0.00519	0.00231	0.00139	ND	0.00652
	U	7.01767	7.05985	7.05494	ND	7.08324
	±	0.02367	0.01290	0.00614	ND	0.01476
SFRE	N	2.03446	2.06599	2.09086	2.11243	2.14293
	±	0.00449	0.00305	0.00216	0.00157	0.00262
	E	4.76390	4.84061	4.89107	4.94660	4.99285
	±	0.00741	0.00275	0.00203	0.00202	0.00582
	U	9.18377	9.27296	9.27767	9.27820	9.30947
	±	0.02764	0.01623	0.01116	0.00846	0.01395
VANI	N	9.42078	9.46442	9.49105	9.51535	ND
	±	0.00267	0.00156	0.00122	0.00140	ND
	E	2.45266	2.54597	2.60689	2.66022	ND
	±	0.00322	0.00164	0.00120	0.00187	ND
	U	2.00303	1.99439	2.02384	1.99901	ND
	±	0.02576	0.00925	0.00651	0.00769	ND

SITE	DIR	1991.563	1994.766	1996.739	1998.711	2000.758
ZECK	N	ND	ND	ND	1.51676	1.53706
	±	ND	ND	ND	0.00040	0.00041
	E	ND	ND	ND	1.55894	1.60892
	±	ND	ND	ND	0.00061	0.00065
	U	ND	ND	ND	6.27418	6.27466
	±	ND	ND	ND	0.00121	0.00138
ZELB	N	1.85230	1.88473	1.90398	ND	ND
	±	0.00157	0.00072	0.00068	ND	ND
	E	0.21499	0.30104	0.35676	ND	ND
	±	0.00227	0.00095	0.00079	ND	ND
	U	5.21060	5.28061	5.26822	ND	ND
	±	0.02157	0.00343	0.00346	ND	ND

Appendix B

Conversion Velocities for ITRF2000 to Eurasian Reference Frame

Velocities (mm/yr) to convert position measurements of each station from the ITRF2000 to a Eurasian reference frame.

CONVERSION VELOCITIES FROM ITRF2000 TO EURASIA

STATION	NORTH (mm/yr)	EAST (mm/yr)
KHOT	9.18	25.67
KHUR	9.12	25.68
LESO	9.09	25.71
NICH	8.86	25.88
SACC	9.12	25.71
SFRE	9.12	25.70
VANI	9.33	25.64
ZECK	9.53	25.35
ZELB	9.53	25.35

Appendix C

GPS Displacements

GPS displacements (in mm) used in postseismic deformation modeling. (a) 1991-1994 without secular correction (b) 1991-1994 with secular correction from time-series. (c) 1991-1994 with secular correction from block model. (d) 1994-1996 without secular correction (e) 1994-1996 with secular correction from time-series. (f) 1994-1996 with secular correction from block model.

1991-1994 NON-CORRECTED (NC) GPS DISPLACEMENTS

	NORTH	σ-N	EAST	σ-E	UP	σ-U
KHOT	20.820	6.108	18.360	20.258	60.080	35.045
KHUR	5.830	4.906	-16.330	6.542	69.730	30.157
LESO	-3.960	4.231	-13.020	6.413	95.990	28.587
NICH	-3.300	3.193	23.970	3.637	87.500	26.637
SACC	5.010	3.758	18.590	5.681	42.180	26.957
SFRE	-5.600	5.428	2.320	7.904	89.190	32.053
VANI	11.190	3.092	13.760	3.614	-8.640	27.370
ZELB	4.860	1.727	1.910	2.461	70.010	21.841

(a)

1991-1994 TIME-SERIES CORRECTED (TSC) GPS DISPLACEMENTS

	NORTH	σ-N	EAST	σ-E	UP	σ-U
KHOT	9.640	6.108	19.773	20.258	39.915	35.045
KHUR	-18.613	4.906	9.545	6.542	55.484	30.157
LESO	-13.259	4.231	-6.825	6.413	82.217	28.587
SACC	0.402	3.758	6.005	5.681	19.628	26.957
SFRE	-10.003	5.428	-4.340	7.904	63.699	32.052
VANI	4.172	3.092	6.692	3.614	31.689	27.370
ZELB	0.544	1.727	3.292	2.461	50.633	21.841

(b)

1991-1994 BLOCK MODEL CORRECTED (BMC) GPS DISPLACEMENTS

	NORTH	σ-N	EAST	σ-E	UP	σ-U
KHOT	8.420	6.108	20.510	20.258	60.080	35.045
KHUR	-22.500	4.906	5.470	6.542	69.730	30.157
LESO	-20.490	4.231	-4.150	6.413	95.990	28.587
NICH	1.620	3.192	-5.380	3.637	87.500	26.637
SACC	7.050	3.758	3.730	5.681	42.180	26.957
SFRE	-5.760	5.428	-5.750	7.904	89.190	32.053
VANI	1.350	3.092	9.330	3.614	-8.640	27.370
ZELB	-0.780	1.727	3.920	2.461	70.010	21.841

(c)

1994-1996 NON-CORRECTED (NC) GPS DISPLACEMENTS

	NORTH	σ-N	EAST	σ-E	UP	σ-U
KHOT	4.41	2.809	1.102	2.697	-13.470	14.661
KHUR	5.640	2.217	1.790	2.205	-11.250	12.102
LESO	1.039	2.009	3.810	2.186	-7.010	9.749
NICH	9.530	1.473	1.165	1.944	-6.630	7.120
SACC	1.220	2.853	1.162	2.696	-4.910	14.287
SFRE	-2.500	3.737	6.870	3.418	4.710	19.697
VANI	1.033	1.980	8.220	2.032	29.450	11.311
ZELB	5.700	0.990	4.400	1.236	-12.390	4.872

(d)

1994-1996 TIME-SERIES CORRECTED (TSC) GPS DISPLACEMENTS

	NORTH	σ-N	EAST	σ-E	UP	σ-U
KHOT	5.653	2.809	3.773	2.697	-25.894	14.661
KHUR	0.386	2.217	7.922	2.206	-20.027	12.102
LESO	3.667	2.009	8.632	2.186	-15.496	9.749
SACC	0.416	2.853	12.820	2.696	-18.805	14.287
SFRE	-0.720	3.737	0.522	3.418	-10.996	19.697
VANI	2.312	1.980	7.551	2.032	54.298	11.311
ZELB	-0.396	0.990	4.730	1.236	-24.327	4.872

(e)

1994-1996 BLOCK MODEL CORRECTED (BMC) GPS DISPLACEMENTS

	NORTH	σ-N	EAST	σ-E	UP	σ-U
KHOT	4.910	2.809	4.220	2.697	-13.470	14.661
KHUR	-2.010	2.217	5.410	2.205	-11.250	12.102
LESO	-0.800	2.009	0.103	2.186	-7.010	9.749
NICH	-2.130	1.473	8.250	1.944	-6.630	7.120
SACC	4.510	2.853	11.420	2.696	-4.910	14.287
SFRE	1.900	3.737	-0.350	3.418	4.710	19.697
VANI	0.580	1.980	9.170	2.032	29.450	11.311
ZELB	-1.210	0.990	5.120	1.236	-12.390	4.872

(f)

Appendix D

Earth Model for Viscoelastic Modeling

Earth model used in viscoelastic forward modeling with the Visco1D program. This 1-D model ranges from the Earth's surface to a depth of 1086.6 km.

Earth Model for Viscoelastic Forward Modeling

DEPTH 1 (km)	DEPTH 2 (km)	DENSITY (g/cm^3)	BULK MOD. ($\times 10^{10}$ Pa)	SHEAR MOD. ($\times 10^{10}$ Pa)
0	3	2.60	3.7	1.77
3	4	2.60	4.17	2.65
4	7	2.60	4.17	2.65
7	8	2.60	5.03	3.2
8	10	2.60	5.03	3.2
10	12	2.60	5.03	3.2
12	15	2.60	5.03	3.2
15	16	2.90	5.61	3.57
16	20	2.90	5.61	3.57
20	25	2.90	5.61	3.57
25	30	2.90	5.61	3.57

DEPTH 1 (km)	DEPTH 2 (km)	DENSITY (g/cm^3)	BULK MOD. ($\times 10^{10}$ Pa)	SHEAR MOD. ($\times 10^{10}$ Pa)
30	35	2.90	5.61	3.57
35	45	2.90	5.61	3.57
45	80	3.38	13.07	6.77
80	113.5	3.37	15.00	7.00
113.5	139.1	3.37	15.00	7.00
139.1	164.7	3.38	15.00	7.00
164.7	190.4	3.39	15.00	7.00
190.4	216.0	3.39	15.00	7.00
216.0	241.6	3.40	15.00	7.00
292.9	267.2	3.42	15.00	7.00
267.2	292.9	3.44	15.00	7.00
292.9	318.5	3.47	15.00	7.00
318.5	344.1	3.51	15.00	7.00
344.1	369.8	3.55	15.00	7.00
369.8	395.4	3.60	15.00	7.00
395.4	421.0	3.66	15.00	7.00
421.0	452.3	3.71	15.00	7.00
452.3	483.5	3.76	15.00	7.00
483.5	514.7	3.81	15.00	7.00
514.7	546.0	3.85	15.00	7.00
546.0	577.2	3.90	15.00	7.00
577.2	608.5	3.96	15.00	7.00
608.5	639.7	4.03	15.00	7.00
639.7	671.0	4.11	15.00	7.00
671.0	705.6	4.21	15.00	7.00
705.6	740.3	4.32	15.00	7.00
740.3	774.9	4.40	15.00	7.00
774.9	809.5	4.47	15.00	7.00
809.5	844.2	4.51	15.00	7.00
844.2	878.8	4.54	15.00	7.00
878.8	913.4	4.54	15.00	7.00
913.4	948.1	4.54	15.00	7.00
948.1	982.7	4.54	15.00	7.00
982.7	1017.3	4.55	15.00	7.00
1017.3	1051.9	4.57	15.00	7.00

DEPTH 1 (km)	DEPTH 2 (km)	DENSITY (g/cm^3)	BULK MOD. ($\times 10^{10}$ Pa)	SHEAR MOD. ($\times 10^{10}$ Pa)
1051.9	1086.6	4.59	15.00	7.00